symmetry

MDPI

Article

Enhancing Heat Transfer in Blood Hybrid Nanofluid Flow with $Ag–TiO_2$ Nanoparticles and Electrical Field in a Tilted Cylindrical W-Shape Stenosis Artery: A Finite Difference Approach

Ebrahem A. Algehyne [1,*], N. Ameer Ahammad [1,*], Mohamed E. Elnair [1], Mohamed Zidan [1], Yasir Y. Alhusayni [1], Babikir Osman El-Bashir [2], Anwar Saeed [3], Ali Saleh Alshomrani [4] and Faris Alzahrani [4]

[1] Department of Mathematics, Faculty of Science, University of Tabuk, Tabuk 71491, Saudi Arabia; abomunzir124@gmail.com (M.E.E.); mabdelwahab@ut.edu.sa (M.Z.); yasser1math@gmail.com (Y.Y.A.)
[2] Department of Physics, Faculty of Science, University of Tabuk, Tabuk 71491, Saudi Arabia; balbashir@ut.edu.sa
[3] Centre of Excellence in Theoretical and Computational Science (TaCS-CoE), Faculty of Science, King Mongkut's University of Technology, Thonburi (KMUTT), Bangkok 10140, Thailand; anwarsaeed769@gmail.com
[4] Mathematical Modelling and Applied Computation Research Group (MMAC), Department of Mathematics, King Abdul Aziz University, Jeddah 21589, Saudi Arabia; aszalshomrani@kau.edu.sa (A.S.A.); falzahrani1@kau.edu.sa (F.A.)
* Correspondence: e.algehyne@ut.edu.sa (E.A.A.); anaudalur@ut.edu.sa (N.A.A.)

Citation: Algehyne, E.A.; Ahammad, N.A.; Elnair, M.E.; Zidan, M.; Alhusayni, Y.Y.; El-Bashir, B.O.; Saeed, A.; Alshomrani, A.S.; Alzahrani, F. Enhancing Heat Transfer in Blood Hybrid Nanofluid Flow with $Ag–TiO_2$ Nanoparticles and Electrical Field in a Tilted Cylindrical W-Shape Stenosis Artery: A Finite Difference Approach. *Symmetry* **2023**, *15*, 1242. https://doi.org/10.3390/sym15061242

Academic Editors: Ranjit Kumar Upadhyay and Ramalingam Udhayakumar

Received: 7 May 2023
Revised: 6 June 2023
Accepted: 8 June 2023
Published: 10 June 2023

Abstract: The present research examines the unsteady sensitivity analysis and entropy generation of blood-based silver–titanium dioxide flow in a tilted cylindrical W-shape symmetric stenosis artery. The study considers various factors such as the electric field, joule heating, viscous dissipation, and heat source, while taking into account a two-dimensional pulsatile blood flow and periodic body acceleration. The finite difference method is employed to solve the governing equations due to the highly nonlinear nature of the flow equations, which requires a robust numerical technique. The utilization of the response surface methodology is commonly observed in optimization procedures. Drawing inspiration from drug delivery techniques used in cardiovascular therapies, it has been proposed to infuse blood with a uniform distribution of biocompatible nanoparticles. The figures depict the effects of significant parameters on the flow field, such as the electric field, Hartmann number, nanoparticle volume fraction, body acceleration amplitude, Reynolds number, Grashof number, and thermal radiation, on velocity, temperature (nondimensional), entropy generation, flow rate, resistance to flow, wall shear stress, and Nusselt number. The velocity and temperature profiles improve with higher values of the wall slip parameter. The flow rate profiles increase with an increment in wall velocity but decrease with the Womersley number. Increasing the intensity of radiation and decreasing magnetic fields both result in a decrease in the rate of heat transfer. The blood temperature is higher with the inclusion of hybrid nanoparticles than the unitary nanoparticles. The total entropy generation profiles increase for higher values of the Brickman number and temperature difference parameters. Unitary nanoparticles exhibit a slightly higher total entropy generation than hybrid nanoparticles, particularly when positioned slightly away from the center of the artery. The total entropy production decreases by 17.97% when the thermal radiation is increased from absence to 3. In contrast, increasing the amplitude of body acceleration from 0.5 to 2 results in a significant enhancement of 76.14% in the total entropy production.

Keywords: heat transfer; EMHD; entropy generation; stenosed artery; finite difference method

1. Introduction

The scientific and engineering communities have shown significant interest in nanotechnology due to its diverse practical applications, particularly in the fields of biology and medicine. A wide range of nanoparticles, such as ferrite, silver, gold, copper, and magnesium oxide, have been utilized in various applications, including protein and nucleic acid manipulation, drug delivery, water treatment, heat transfer systems, vaccination, catalysis, antimicrobial activity, and gene transportation [1–9]. Due to their exceptional biocompatibility, magnetic properties, chemical properties, specific mechanical properties, and thermal efficiency, these materials have garnered significant attention in academic circles [10,11]. In the realm of medical applications, silver nanoparticles (atomic number = 47) and titanium dioxide (atomic number = 38) have been observed to be highly prevalent compared to other nanoparticles. This is due to their exceptional quenching efficiencies, imaging capabilities, targeting ligands, probes, and significant surface modifiability, which make them suitable for ribonucleic acid quantification via optical biosensors and treating malignant tumors. The utilization of silver (Ag) and titanium dioxide (TiO_2) in diverse medical applications has been investigated owing to their distinctive characteristics and possible synergistic outcomes. The potential application of Ag–TiO_2 nanocomposites in cancer therapy has been investigated. The nanocomposites possess the ability to function as photothermal agents, whereby they can effectively assimilate light and subsequently convert it into thermal energy, thereby facilitating the eradication of cancerous cells. The incorporation of Ag and TiO_2 within the nanocomposite has been observed to augment the efficacy of the photothermal effect [12]. The utilization of contrast agents in diagnostic imaging techniques has also been investigated. The coexistence of Ag and TiO_2 within the nanocomposite has the potential to augment contrast in imaging modalities such as CT and MRI. The evidence suggests that it possesses promising capabilities for use in the context of wound healing [13,14]. Nanocomposites possess the potential to function as antibacterial agents and facilitate the processes of tissue regeneration and angiogenesis, the latter of which pertains to the generation of novel blood vessels. It has the potential to serve as a vehicle for the transportation of pharmaceutical agents. The incorporation of Ag and TiO_2 within the nanocomposite material has been shown to yield improved drug loading capabilities and regulated drug release. The impact of the flow of a hybrid nanofluid consisting of Ag–TiO_2 over a slender needle under the influence of a magnetic field and thermal radiation was investigated by Nazar et al. [15]. The study conducted by Kot and Elmaboud [16] investigated the flow characteristics of a hybrid nanofluid consisting of gold and titanium oxide through a vertical artery afflicted with disease, while taking into account the presence of a catheter tube and heat transfer.

The World Health Organization (WHO) research states that cardiovascular diseases (CVDs) continue to be the leading cause of mortality worldwide, accounting for an estimated 17.9 million (nearly 31%) deaths in 2019. It is anticipated that the prevalence of cardiovascular diseases (CVDs) will escalate in the foreseeable future owing to demographic shifts toward an aging population, alterations in lifestyle patterns, and an upsurge in the incidence of obesity and diabetes. Cardiovascular diseases (CVDs) are a cluster of medical conditions that impact the cardiovascular system, encompassing the heart and blood vessels. Numerous risk factors have been identified as potential contributors to the onset of cardiovascular diseases (CVDs). These include an unhealthy diet, insufficient physical activity, tobacco use, elevated blood pressure and cholesterol levels, obesity, diabetes, and a family history of CVDs, among others. Cardiovascular diseases (CVDs) have the potential to inflict harm upon various components of the cardiovascular system, such as the heart, blood vessels, and other organs [16–20]. This can occur as a result of conditions such as coronary artery disease, heart failure, peripheral artery disease, aortic aneurysms, and arrhythmias [21]. The main cause of such diseases is the accumulation of cholesterol and low-density lipoproteins within the lumen, which leads to atherosclerosis or the hardening of the arteries. The formation of a plaque leads to the subsequent constriction of the arterial area, resulting in hemodynamic stenosis. This stenosis, in turn, causes a reduction in the blood supply to various organs within the body. The composition of human blood is characterized by a heterogeneous multiphase suspension of different blood cells, including erythrocytes, leukocytes, and platelets, which are suspended in plasma. The scientific consensus is that plasma conforms to the Newtonian fluid model. Nevertheless, suspensions in whole blood result in non-Newtonian fluid behavior, leading to significant changes in its rheological properties [22,23].

Energy cannot be generated or destroyed; it can only be transferred or changed from one form to another, according to the first rule of thermodynamics, often known as the principle of energy conservation. The aforementioned law is a fundamental principle in physics and applies to all thermodynamic processes, encompassing those that involve internal energy, work, and heat. The concept of entropy generation is closely linked to the first law of thermodynamics, as it quantifies the energy that is dissipated or lost due to irreversible processes within a given system. Stated differently, the concept of entropy generation pertains to the fraction of energy incapable of being transformed into productive work owing to the inadequacies inherent in actual processes [24,25]. The first law of thermodynamics postulates energy conservation, whereas the subsequent law acknowledges the dissipation of a portion of this energy due to entropy generation [26]. Entropy generation is a phenomenon commonly linked to irreversible processes that take place within a thermodynamic system. Such processes include friction, heat transfer across a finite temperature gradient, and mixing of different substances. These processes result in a rise in the level of entropy within the system and a reduction in the amount of work that can be extracted from the system. The concept of entropy generation holds significant importance in the fields of engineering and thermodynamics, as it serves as a fundamental constraint on the efficacy of energy conversion procedures [27,28]. In the context of a heat engine, a portion of the energy input is inevitably dissipated due to irreversibilities. This phenomenon induces a rise in entropy and a concomitant reduction in the quantity of work that can be derived from the system. Comprehending and mitigating entropy generation is of utmost importance in enhancing the efficacy of energy conversion mechanisms and curbing wastage [29–32].

The present investigation is motivated by the practical significance of nano-drug delivery methods and aims to address the management of treatment options for arterial disease through numerical simulations. Numerical blood flow simulations have emerged as valuable tools for supporting decision-making processes in cardiovascular disease treatment. While conventional approaches typically involve stents or catheters placed inside the affected artery, there is a growing trend toward targeted delivery of nano-drugs to specific locations. This approach also involves the initiation of blood clot formation at narrowed sections of the artery, and computational simulations can be employed to predict the impact of these post-treatment processes. Numerous previous studies have explored blood flow in stenosed arteries with variations in shape, size, and other characteristics, as evidenced by the aforementioned research. In the present investigation, the focus is on analyzing the analysis and entropy generation of a blood hybrid nanofluid flow containing silver–titanium dioxide nanoparticles within a tilted cylindrical W-shaped stenosed artery using electromagnetohydrodynamic principles. Furthermore, the principal applications of silver–titanium dioxide nanoparticles encompass targeted drug delivery, wound management, cancer detection, cardiovascular therapy, and chemotherapy. The current framework focuses on the flow of a biomagnetic silver–titanium dioxide blood hybrid nanofluid in a W-shape inclined stenosis artery. The framework takes into account motivating factors and incorporates time-dependent sensitivity analysis and entropy creation using variable viscosity and Lorentz force. The two-dimensional governing equations were subjected to moderate stenotic approximation after normalizing relevant variables. The FTCS method was employed due to the considerably nonlinear nature of the resulting dimensionless boundary value problem, necessitating a dependable numerical approach.

2. Mathematical Formulation

This study focuses on a mathematical model that analyzes the flow of a time-dependent, two-dimensional blood-based hybrid nanofluid. The model specifically examines the flow of silver–titanium dioxide nanoparticles in a slanted artery with W-shape symmetric stenosis, as shown in Figure 1. The study uses a nanoparticle volume fraction model to analyze the biomagnetic blood flow. It is important to note that the blood fluid being analyzed contains both silver and titanium dioxide nanoparticles. The direction of blood flow is opposite to the direction of the strongest Lorentz force. The arterial radial and axial coordinates are represented by r and z in this modeling, which uses the two-dimensional cylindrical coordinate system (r, θ, z) [33–37]. The present study focuses on the analysis of an electrically conducting incompressible unsteady blood hybrid nanofluid. A modified Tiwari–Das nanoscale model is employed, allowing for the determination of unique properties of the actual nanoparticles, such as viscosity, thermal conductivity, specific heat capacity, and density. The flow equation takes into account the influence of body force. Since the induced magnetic field strength is relatively small compared to the external magnetic field (resulting in a small magnetic Reynolds number), it is neglected in the analysis. Additionally, Hall current, ion slip, and Maxwell displacement currents are also disregarded. Viscous dissipation and joule heating, however, are considered in the energy equation. Given the unsteady nature of blood flow, pulsatile pressure gradient and wall slip effects in streaming blood are taken into consideration as well.

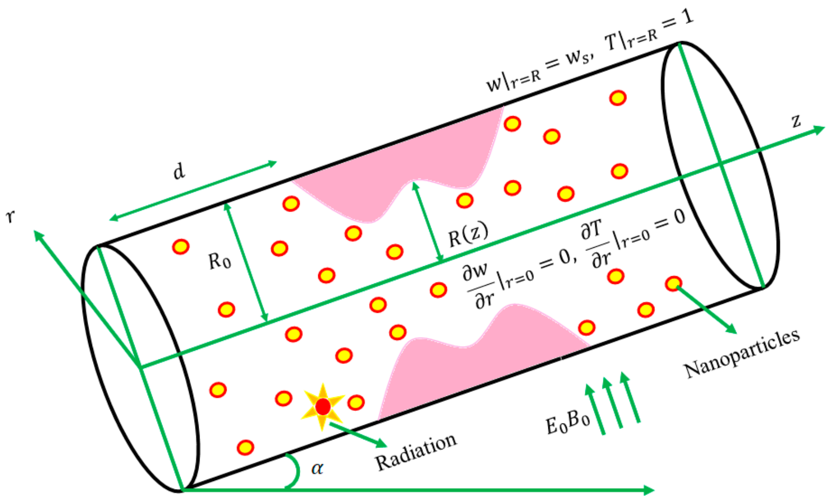

Figure 1. Physical configuration of the problem.

W-shape stenosis symmetric [36]:

$$\left.\begin{array}{ll} R_0\left[1-\frac{64}{10}\eta\left(\frac{11}{32}l_0^3(z-d)-\frac{47}{48}l_0^2(z-d)^2+l_0(z-d)^2-\frac{1}{3}(z-d)^4\right)\right], & \bar{d}\le\bar{z}\le\bar{d}+\frac{3}{2}\,l_0 \\ R_0 \quad\quad \text{otherwise} & \end{array}\right\} = R(z) \tag{1}$$

Flow equations are presented by [33–37].

$$\frac{\partial\overline{u}}{\partial\overline{r}}+\frac{\overline{u}}{\overline{r}}+\frac{\partial\overline{w}}{\partial\overline{z}}=0, \tag{2}$$

$$\begin{gathered} \rho_{hnf}\left(\frac{\partial\overline{u}}{\partial\overline{t}}+\overline{u}\frac{\partial\overline{u}}{\partial\overline{r}}+\overline{w}\frac{\partial\overline{u}}{\partial\overline{z}}\right)=-\frac{\partial P}{\partial\overline{r}}+\frac{1}{\overline{r}}\frac{\partial}{\partial\overline{r}}\left(\mu_{hnf}(T)\frac{\partial\overline{u}}{\partial\overline{r}}\right)-2\mu_{hnf}(T)\left(\frac{\overline{u}}{\overline{r}^2}\right) \\ +\frac{\partial}{\partial\overline{z}}\left(\mu_{hnf}(T)\left(\frac{\partial\overline{u}}{\partial\overline{z}}+\frac{\partial\overline{w}}{\partial\overline{r}}\right)\right)+g(\gamma\rho)_{hnf}(T-T_1)\cos\alpha \end{gathered} \tag{3}$$

$$\begin{gathered} \rho_{hnf}\left(\frac{\partial\overline{w}}{\partial\overline{t}}+\overline{u}\frac{\partial\overline{w}}{\partial\overline{r}}+\overline{w}\frac{\partial\overline{w}}{\partial\overline{z}}\right)=-\frac{\partial P}{\partial\overline{z}}+\frac{1}{\overline{r}}\frac{\partial}{\partial\overline{r}}\left(\overline{r}\,\mu_{hnf}(T)\left(\frac{\partial\overline{u}}{\partial\overline{z}}+\frac{\partial\overline{w}}{\partial\overline{r}}\right)\right) \\ +g(\gamma\rho)_{hnf}(T-T_1)\sin\alpha+\frac{\partial}{\partial\overline{z}}\left(2\mu_{hnf}(T)\frac{\partial\overline{w}}{\partial\overline{z}}\right) \\ +\rho_{hnf}G(t)-\sigma_{hnf}\left(B_0^2\overline{w}-E_0B_0\right) \end{gathered} \tag{4}$$

$$(\rho C_p)_{hnf}\left(\frac{\partial T}{\partial \bar{t}}+\bar{u}\frac{\partial T}{\partial \bar{r}}+\bar{w}\frac{\partial T}{\partial \bar{z}}\right)=k_{hnf}\left(\frac{\partial^2 T}{\partial \bar{r}^2}+\frac{1}{\bar{r}}\frac{\partial T}{\partial \bar{r}}+\frac{\partial^2 T}{\partial \bar{z}^2}\right)-\frac{\partial q_r}{\partial \bar{r}}$$
$$+\sigma_{hnf}(B_0\bar{w}-E_0B_0)^2+Q_0 \quad (5)$$
$$+\mu_{hnf}\left[2\left(\frac{\partial \bar{u}}{\partial \bar{r}}\right)^2+2\left(\frac{\bar{u}}{\bar{r}}\right)^2+\left(\frac{\partial \bar{u}}{\partial \bar{z}}+\frac{\partial \bar{w}}{\partial \bar{r}}\right)^2+2\left(\frac{\partial \bar{w}}{\partial \bar{z}}\right)^2\right]$$

Boundary conditions [35–37]:

$$\left.\begin{array}{l} w(R,t)=w_S,\frac{\partial w(0,t)}{\partial r}=0, w(r,0)=0,\\ T(R,t)=1,\frac{\partial T(0,t)}{\partial r}=0, T(r,0)=0. \end{array}\right\} \quad (6)$$

Table 1 discloses the initial and boundary condition of the present model. Table 2 provides the thermophysical characteristics of the base fluid (blood) and the nanomaterials (silver–titanium dioxide. The nonlinear flow equations governing the system are subjected to a transformation using appropriate nonsimilar variables, as demonstrated below [33–37].

$$r=\frac{\bar{r}}{R_0}, z=\frac{\bar{z}}{l_0}, \bar{p}=\frac{R_0^2P}{U_0l_0\mu_f}, u=\frac{l_0\bar{u}}{\delta^* U_0}, \theta=\frac{T-T_1}{T_w-T_1},$$
$$w=\frac{\bar{w}}{U_0}, R=\frac{\bar{R}}{R_0}, t=\frac{U_0\bar{t}}{R_0}, d=\frac{\bar{d}}{l_0}. \quad (7)$$

Table 1. Initial and boundary condition of the present model [35–37].

Conditions		Velocity	Temperature
Initial $t=0$		$w=0$	$T=0$
Boundary	$r=0$	$\frac{\partial w}{\partial r}=0$	$\frac{\partial T}{\partial r}=0$
	$r=R$	$w=w_S$	$T=1$

Table 2. The values pertaining to the different physical parameters [36,37].

Physical Properties	Blood	Ag	TiO_2
$\rho\left(\frac{kg}{m^3}\right)$	1050	10,500	4250
$C_p\left(\frac{J}{kg\ K}\right)$	3617	235	686.2
$k\left(\frac{W}{m\ K}\right)$	0.52	429	8.9538
$\gamma\left(\frac{1}{K}\right)\times 10^{-5}$	0.18	1.89	0.9
$\sigma(S/m)$	6.67×10^{-1}	6.3×10^{7}	2.38×10^{6}

The utilization of the aforementioned variables in Equations (2)–(5) results in the following transformed equations:

$$\delta\left(\frac{\partial u}{\partial r}+\frac{u}{r}\right)+\frac{\partial w}{\partial z}=0, \quad (8)$$

$$\mathrm{R_e}\left(\frac{\rho_{hnf}}{\rho_f}\right)\delta\varepsilon^2\left(\frac{\partial u}{\partial t}+(\delta\varepsilon)u\frac{\partial u}{\partial r}+\varepsilon w\frac{\partial u}{\partial z}\right)=-\frac{\partial p}{\partial r}$$
$$+\left(\frac{\delta R_0}{l_0^2\mu_0}\right)\frac{1}{r}\frac{\partial}{\partial r}\left(\mu_{hnf}(\theta)\frac{\partial u}{\partial r}\right)+\left(\frac{\varepsilon^2 R_0}{\mu_0}\right)\frac{\partial}{\partial z}\left(\mu_{hnf}(\theta)\left(\frac{\delta\varepsilon}{l_0}\frac{\partial u}{\partial z}+\frac{1}{R_0}\frac{\partial w}{\partial r}\right)\right) \quad (9)$$
$$-2\left(\frac{\delta\varepsilon^2}{\mu_0}\right)\mu_{hnf}(\theta)\left(\frac{u}{r^2}\right)+\left(\frac{(\rho\gamma)_{hnf}}{(\rho\gamma)_f}\right)\varepsilon\cos(\alpha)G_r\theta,$$

$$\begin{aligned}&\mathrm{R_e}\left(\frac{\rho_{hnf}}{\rho_f}\right)\left(\frac{\partial w}{\partial t}+(\delta\varepsilon)u\frac{\partial w}{\partial r}+\varepsilon w\frac{\partial w}{\partial z}\right)=-\frac{\partial p}{\partial z}\\&+\frac{1}{r}\frac{\partial}{\partial r}\left(\frac{r\mu_{hnf}(\theta)}{\mu_0}\left\{\delta\varepsilon^2\frac{\partial u}{\partial z}+\frac{\partial w}{\partial r}\right\}\right)+\left(\frac{\rho_{hnf}}{\rho_f}\right)G(t)-\frac{\sigma_{hnf}}{\sigma_f}M_a^2(w-E_1)\\&+\varepsilon^2\frac{\partial}{\partial z}\left(\frac{2\mu_{hnf}(\theta)}{\mu_0}\frac{\partial w}{\partial z}\right)+\left(\frac{(\rho\gamma)_{hnf}}{(\rho\gamma)_f}\right)G_r\theta\sin(\alpha)\end{aligned}\tag{10}$$

$$\begin{aligned}&\left(\frac{(\rho C_p)_{hnf}}{(\rho C_p)_f}\right)\left(\frac{\partial\theta}{\partial t}+(\delta\varepsilon)u\frac{\partial\theta}{\partial r}+\varepsilon w\frac{\partial\theta}{\partial z}\right)=\frac{k_{hnf}}{k_f\mathrm{Pr}\,R_e}\left(\frac{\partial^2\theta}{\partial r^2}+\frac{1}{r}\frac{\partial\theta}{\partial r}+\varepsilon^2\frac{\partial^2\theta}{\partial z^2}\right)\\&+\frac{Q}{\mathrm{Pr}\,R_e}+\left(\frac{\sigma_{hnf}}{\sigma_f}\right)\frac{E_CM_a^2}{\mathrm{R_e}}(w-E_1)^2+\frac{N_R}{\mathrm{Pr}\,R_e}\frac{\partial^2\theta}{\partial r^2}\\&+\left(\frac{\mu_{hnf}}{\mu_f}\right)\frac{E_C}{R_e}\left(2\delta^2\varepsilon^2\left(\frac{\partial u}{\partial r}\right)^2+2\varepsilon^2\left(\frac{\partial w}{\partial z}\right)^2+2\delta^2\varepsilon^2\left(\frac{u}{r}\right)^2+\left(\delta\varepsilon^2\frac{\partial u}{\partial z}+\frac{\partial w}{\partial r}\right)^2\right).\end{aligned}\tag{11}$$

Here, $\Lambda=\frac{\rho_f\omega R_0^2}{2\pi\mu_f}$ is the Womersley number, U_0 mathvariant="normal", $M_a^2=\frac{\sigma_f}{\mu_f}B_0^2R_0^2$ is the Hartmann number, $G_r=\frac{g\rho_fR_0^2\gamma_f(T_w-T_1)}{U_0\mu_f}$ is the Grashof number, $\mathrm{R_e}=\frac{U_0\rho_fR_0}{\mu_f}$ is the Reynolds number, $E_C=\frac{U_0^2}{(C_p)_f(T_w-T_1)}$ is the Eckert number, T_w is the wall temperature, $\varepsilon=\frac{R_0}{l_0}$ is the vessel aspect ratio, $N_R=\frac{16\sigma_eT_1^3}{3k_fk_e}$ thermal radiation, $Pr=\frac{(C_p)_f\mu_f}{k_f}$ is the Prandtl number, and $\delta=\frac{\delta^*}{R_0}$ is the stenosis height parameter.

The thermophysical properties of hybrid nanofluids and nanofluids are described in [34,36].

$$\left.\begin{aligned}&\frac{\mu_{hnf}}{\mu_f}=\frac{1}{(1-\phi_{Ag})^{2.5}(1-\phi_{Tio_2})^{2.5}},\alpha_{hnf}=\frac{k_{hnf}}{(\rho C_p)_{hnf}},\\&\frac{\rho_{hnf}}{\rho_f}=(1-\phi_{Tio_2})\left(\left(1-\phi_{Ag}\right)+\phi_{Ag}\frac{\rho_{Ag}}{\rho_f}\right)+\phi_{Tio_2}\frac{\rho_{Tio_2}}{\rho_f},\\&\frac{(\rho C_p)_{hnf}}{(\rho C_p)_f}=(1-\phi_{Tio_2})\left(\left(1-\phi_{Ag}\right)+\phi_{Ag}\frac{(\rho C_p)_{Ag}}{(\rho C_p)_f}\right)+\phi_{Tio_2}\frac{(\rho C_p)_{Tio_2}}{(\rho C_p)_f},\\&\frac{(\rho\gamma)_{hnf}}{(\rho\gamma)_f}=(1-\phi_{Tio_2})\left(\left(1-\phi_{Ag}\right)+\phi_{Ag}\frac{(\rho\gamma)_{Ag}}{(\rho\gamma)_f}\right)+\phi_{Tio_2}\frac{(\rho\gamma)_{Tio_2}}{(\rho\gamma)_f},\\&\frac{k_{hnf}}{k_{bf}}=\frac{(1+2\phi_{Tio_2})k_{Tio_2}+2(1-\phi_{Tio_2})k_{bf}}{(1-\phi_{Ta})k_{Tio_2}+(2+\phi_{Tio_2})k_{bf}},where\frac{k_{bf}}{k_f}=\frac{(1+2\phi_{Ag})k_{Ag}+2(1-\phi_{Ag})k_f}{(1-\phi_{Au})k_{Ag}+(2+\phi_{Ag})k_f}\\&\frac{\sigma_{hnf}}{\sigma_{bf}}=\frac{\sigma_{Tio_2}+2\sigma_{bf}-2\phi_{Tio_2}(\sigma_{bf}-\sigma_{Tio_2})}{\sigma_{Tio_2}+2\sigma_{bf}+\phi_{Tio_2}(\sigma_{bf}-\sigma_{Tio_2})},where\ \frac{\sigma_{bf}}{\sigma_f}=\frac{\sigma_{Ag}+2\sigma_f-2\phi_{Ag}(\sigma_f-\sigma_{Ag})}{\sigma_{Ag}+2\sigma_f+\phi_{Ag}(\sigma_f-\sigma_{Ag})}.\end{aligned}\right\}\tag{12}$$

$$\left.\begin{aligned}&\frac{\mu_{nf}}{\mu_f}=\frac{1}{(1-\phi_{Ag})^{2.5}},\alpha_{hnf}=\frac{k_{nf}}{(\rho C_p)_{nf}},\frac{\sigma_{nf}}{\sigma_f}=\frac{\sigma_{Ag}+2\sigma_f-2\phi_{Ag}(\sigma_f-\sigma_{Ag})}{\sigma_{Ag}+2\sigma_f+\phi_{Ag}(\sigma_f-\sigma_{Ag})},\\&\frac{\rho_{nf}}{\rho_f}=\left(\left(1-\phi_{Ag}\right)+\phi_{Ag}\frac{\rho_{Ag}}{\rho_f}\right),\frac{(\rho C_p)_{nf}}{(\rho C_p)_f}=\left(\left(1-\phi_{Ag}\right)+\phi_{Ag}\frac{(\rho C_p)_{Ag}}{(\rho C_p)_f}\right),\\&\frac{(\rho\gamma)_{nf}}{(\rho\gamma)_f}=\left(\left(1-\phi_{Ag}\right)+\phi_{Ag}\frac{(\rho\gamma)_{Ag}}{(\rho\gamma)_f}\right),\frac{k_{nf}}{k_f}=\frac{(1+2\phi_{Ag})k_{Ag}+2(1-\phi_{Ag})k_f}{(1-\phi_{Au})k_{Ag}+(2+\phi_{Ag})k_f}\end{aligned}\right\}\tag{13}$$

The viscosity of blood within a biological system is subject to fluctuations due to various factors, such as hemoglobin ratio, the vessel dimension, heat, and axial forces or radial directions. Differences in viscosity can give rise to diverse physiological phenomena, including diminished blood viscosity, augmented blood perfusion, decreased coagulation elements, and improved blood circulation. The present model incorporates the influence of temperature on the viscosity of blood nanofluid to effectively capture the aforementioned phenomena. The determining factor is provided by the temperature of the fluid [36,37].

$$\mu_f(\theta) = \mu_0 e^{-\beta_0\theta}, \text{where } e^{-\beta_0\theta} = 1 - \beta_0\theta, \beta_0 \ll 1. \tag{14}$$

The following equation can be used to represent the axial pressure gradient that appears in the above equation [38].

$$-\frac{\partial p}{\partial z} = A_0 + A_1 t \cos(2\pi w_p), t > 0, \tag{15}$$

By using nonsimilar variables, the pressure gradient may be simplified to the following form:

$$-\frac{\partial p}{\partial z} = (e\cos(c_1 t) + 1)B_1, \tag{16}$$

where $B_1 = \frac{A_0 a^2}{\mu_0 U_0}$, $e = \frac{A_1}{A_0}$, and $c_1 = \frac{2\pi a w_p}{U_0}$.

According to the present paradigm, the human body acceleration is expressed as [39]:

$$G(t) = a_g(\cos(\omega_b t + \kappa)) \tag{17}$$

Equation (7) is used to transform Equation (17) into its dimensionless version, which is as follows:

$$G(t) = B_2(\cos(c_2 t + \kappa)) \tag{18}$$

In the equation above, κ stands for the lead angle to the heartbeat, $c_2 = \frac{\omega_b}{\omega}$ for body force, and $B_2 = \rho_f a_g \frac{R_0^2}{\mu_f U_0}$ for body acceleration amplitude.

The findings indicate that the maximum height of stenosis is relatively small in comparison to the radius of the artery. Additionally, the dimensions of the stenotic segment and the radius of the artery are of similar order of magnitude. Consequently, the dimensionless equations governing the flow are minimized under the assumption $\delta \ll 1$ and $\varepsilon = O(1)$. The reduced equations are obtained by utilizing these hypotheses.

$$\frac{\partial w}{\partial z} = 0, \tag{19}$$

$$\frac{\partial p}{\partial r} = 0, \tag{20}$$

$$\begin{aligned} \mathrm{R_e}\left(\frac{\rho_{hnf}}{\rho_f}\right)\left(\Lambda\frac{\partial w}{\partial t}\right) &= B_1(1 + e\cos(c_1 t)) + \frac{1}{r}\frac{\partial}{\partial r}\left(\frac{r\mu_{hnf}(\theta)}{\mu_0}\left(\frac{\partial w}{\partial r}\right)\right) \\ &+ \left(\frac{\rho_{hnf}}{\rho_f}\right)B_2(\cos(c_2 t + \kappa)) + \left(\frac{(\rho\gamma)_{hnf}}{(\rho\gamma)_f}\right)G_r\theta\sin(\alpha) - \frac{\sigma_{hnf}}{\sigma_f}M_a^2(w - E_1), \end{aligned} \tag{21}$$

$$\begin{aligned} \left(\frac{(\rho C_p)_{hnf}}{(\rho C_p)_f}\right)\left(\frac{\partial\theta}{\partial t}\right) &= \frac{1}{\mathrm{Pr}\ R_e}\left(\frac{k_{hnf}}{k_f}\right)\left(\frac{\partial^2\theta}{\partial r^2} + \frac{1}{r}\frac{\partial\theta}{\partial r}\right) + \frac{N_R}{\mathrm{Pr}\ R_e}\frac{\partial^2\theta}{\partial r^2} \\ &+ \left(\frac{\sigma_{hnf}}{\sigma_f}\right)\frac{E_C M_a^2}{\mathrm{R_e}}(w - E_1)^2 + \left(\frac{\mu_{hnf}(\theta)}{\mu_f}\right)\frac{E_C}{\mathrm{R_e}}\left(\frac{\partial w}{\partial r}\right)^2. \end{aligned} \tag{22}$$

The system of equations has been converted into the radial coordinate $(x = r/R(z))$ representation, as the governing flow equations have been integrated with constraining conditions.

$$\begin{aligned} \mathrm{R_e}\left(\frac{\rho_{hnf}}{\rho_f}\right)\left(\Lambda\frac{\partial w}{\partial t}\right) &= B_1(1 + e\cos(c_1 t)) \\ &+ \frac{\mu_{hnf}}{\mu_f}\frac{1}{R^2}\left((1 - \beta_0\theta)\left(\frac{\partial^2 w}{\partial x^2} + \frac{1}{x}\frac{\partial w}{\partial x}\right) - \beta_0\frac{\partial\theta}{\partial x}\frac{\partial w}{\partial x}\right) \\ &+ \left(\frac{\rho_{hnf}}{\rho_f}\right)B_2(\cos(c_2 t + \kappa)) + \left(\frac{(\rho\gamma)_{hnf}}{(\rho\gamma)_f}\right)G_r\theta\sin(\alpha) - \frac{\sigma_{hnf}}{\sigma_f}M_a^2(w - E_1), \end{aligned} \tag{23}$$

$$\left(\frac{(\rho C_p)_{hnf}}{(\rho C_p)_f}\right)\left(\frac{\partial\theta}{\partial t}\right) = \frac{1}{\Pr R_e}\left(\frac{k_{hnf}}{k_f}\right)\left(\frac{1}{R^2}\right)\left(\frac{\partial^2\theta}{\partial x^2} + \frac{1}{x}\frac{\partial\theta}{\partial x}\right)$$
$$+\left(\frac{1}{R^2}\right)\frac{N_R}{\Pr R_e}\frac{\partial^2\theta}{\partial x^2} + \frac{Q}{\Pr R_e} + \left(\frac{\sigma_{hnf}}{\sigma_f}\right)\frac{E_C M_a^2}{\mathrm{R}_e}(w - E_1)^2 \tag{24}$$
$$+\left(\frac{\mu_{hnf}(\theta)}{\mu_0}\right)\frac{E_C}{\mathrm{R}_e}\left(\frac{\partial w}{\partial x}\right)^2\left(\frac{1}{R^2}\right).$$

Parameters of hemodynamics, such as wall shear stress (τ_s), resistance impedance (λ), Nusselt number (Nu), and volumetric flow rate (Q_F), are formulated mathematically as

$$\left.\begin{aligned} &\tau_s = \frac{1}{R(z)}\left(\frac{\partial w}{\partial x}\right)_{x=1}, \\ &\lambda = L\left[\frac{\left(\frac{\partial p}{\partial z}\right)}{Q_F}\right] = L\left[\frac{B_1(1+e\cos(2\pi t))}{(R(z))^2 2\pi\left(\int_0^1 wxdx\right)}\right], \\ &Nu = \frac{1}{R(z)}\left(\frac{\partial\theta}{\partial x}\right)_{x=1}, \; Q_F = (R(z))^2 2\pi\left(\int_0^1 wxdx\right). \end{aligned}\right\} \tag{25}$$

3. Entropy Generation

Thermal irreversibility, joule heating irreversibility, and fluid friction irreversibility all contribute to the current model's entropy creation [33,34].

$$E_g = \frac{k_f}{T_1^2}\left[\frac{k_{hnf}}{k_f} + \frac{16\sigma_e T_1^3}{3k_f k_e}\right]\left(\frac{\partial T}{\partial \bar r}\right)^2 + \frac{\mu_{hnf}}{T_1}\left[2\left(\left(\frac{\partial \bar u}{\partial \bar r}\right)^2 + \left(\frac{\partial \bar w}{\partial \bar z}\right)^2 + \left(\frac{\bar u}{\bar r}\right)^2\right) + \left(\frac{\partial \bar u}{\partial \bar z} + \frac{\partial \bar w}{\partial \bar r}\right)^2\right] + \frac{\sigma_{hnf}\left(B_0\bar w^2 - E_0 B_0\right)^2}{T_1} \tag{26}$$

By using a dimensionless variable and a radial coordinate, one may create a dimensionless form of entropy.

$$N_g = \left[\frac{k_{hnf}}{k_f} + N_R\right]\left(\frac{1}{R}\right)\left(\frac{\partial\theta}{\partial x}\right)^2 + \left(\frac{1}{R}\right)\frac{\mu_{hnf}}{\mu_f}\frac{Br}{\Omega}\left(\frac{\partial w}{\partial x}\right)^2 + \frac{\sigma_{hnf}}{\sigma_f}\frac{M_a^2 Br(w - E_1)^2}{\Omega} \tag{27}$$

where $\Omega = \frac{T_w - T_1}{T_1}$, temperature difference, $N_g = \frac{{T_1}^2 R_0^2}{k_f(T_w - T_1)^2}E_g$ dimensionless entropy generation, and $Br = \frac{U_0^2\,\mu_f}{k_f(T_w - T_1)}$ Brickman number.

4. Numerical Method

Deriving analytical solutions for the nonlinear equations is challenging, if not impossible (Equations (24) and (25)). In order to solve the problem, a suitable numerical approach is used. This approach is forward in time (FT) and central in space (CS), and it is well described in [10] with further examples of medical flow applications in [11]. Therefore, in computational fluid dynamics, it is usually referred to as the FTCS difference algorithm. The value of w at node x_i is designated as ω_i^k, and the k^{th} time instant is designated as t^k.

The finite difference formulation of numerous partial derivatives is provided as follows in this notation:

$$\text{Time in Forward}: \frac{\partial w}{\partial t} \cong \frac{w_j^{i+1} - w_j^i}{\Delta t}; \frac{\partial\theta}{\partial t} \cong \frac{\theta_j^{i+1} - \theta_j^i}{\Delta t}$$

$$\text{Space in Central}: \begin{cases} \frac{\partial w}{\partial x} \cong \frac{w_{j+1}^i - w_{j-1}^i}{2\Delta x}; \frac{\partial\theta}{\partial x} \cong \frac{\theta_{j+1}^i - \theta_{j-1}^i}{2\Delta x} \\ \frac{\partial^2 w}{\partial x^2} \cong \frac{w_{j+1}^i - 2w_j^i + w_{j-1}^i}{2\Delta x}; \frac{\partial^2\theta}{\partial x^2} \cong \frac{\theta_{j+1}^i - 2\theta_j^i + \theta_{j-1}^i}{2\Delta x} \end{cases}$$

Using the aforementioned derivative equations, Equations (24) and (25) are easily simplified to the following form:

$$w_j^{i+1} = w_j^i + \frac{\Delta t}{\Lambda \, \mathrm{R_e}\left(1-\phi_2\left[(1-\phi_1)+\phi_1\left(\frac{\rho_{s_1}}{\rho_f}\right)\right]+\phi_2\frac{\rho_{s_2}}{\rho_f}\right)}$$

$$\left[\begin{array}{l} +\left(1-\phi_2\left[(1-\phi_1)+\phi_1\left(\frac{(\rho\gamma)_{s_1}}{(\rho\gamma)_f}\right)\right]+\phi_2\frac{(\rho\gamma)_{s_2}}{(\rho\gamma)_f}\right) \\ G_r\theta_j^i\sin(\alpha)+B_1\left(1+e\cos\left(c_1t^i\right)\right)-\frac{\sigma_{hnf}}{\sigma_f}M_a^2\left(w_j^i-E_1\right) \\ +\frac{\left(1-\beta_0\theta_j^i\right)}{(1-\phi_1)^{2.5}(1-\phi_2)^{2.5}}\left(\frac{1}{R^2}\right)\left(\frac{\partial^2 w}{\partial x^2}+\frac{1}{x}\frac{\partial w}{\partial x}\right) \\ -\frac{\beta_0}{R^2\left((1-\phi_1)^{2.5}(1-\phi_2)^{2.5}\right)}\frac{\partial\theta}{\partial x}\frac{\partial w}{\partial x}+\left(\frac{\rho_{hnf}}{\rho_f}\right)B_2\left(\cos\left(c_2t^i+\kappa\right)\right) \end{array}\right],$$

$$\theta_j^{i+1} = \theta_j^i + \frac{\Delta t}{\left(\frac{(\rho C_p)_{hnf}}{(\rho C_p)_f}\right)}\left[\begin{array}{l} \frac{1}{\Pr R_e}\left(\frac{k_{hnf}}{k_f}\right)\left(\frac{1}{R^2}\right)\left(\frac{\partial^2\theta}{\partial x^2}+\frac{1}{x}\frac{\partial\theta}{\partial x}\right) \\ +\left(\frac{1}{R^2}\right)\frac{N_R}{\Pr R_e}\frac{\partial^2\theta}{\partial x^2} \\ +\left(\frac{\sigma_{nf}}{\sigma_f}\right)\frac{E_C M_a^2}{\mathrm{R_e}}\left(w_j^i-E_1\right)^2 \\ +\left(\frac{\mu_{nf}\left(\theta_j^i\right)}{\mu_0}\right)\frac{E_C}{\mathrm{R_e}}\left(\frac{\partial w}{\partial x}\right)^2\left(\frac{1}{R^2}\right) \end{array}\right]$$

Because the scheme's stability is wholly contingent on the time increment (Δt) and the step size (Δx), the Δt = 0.00001 and Δx = 0.025 are specified in order to address the stability constraint. These values have been shown to be appropriate for stability and convergence of the FTCS method in a number of investigations [36,37,39,40]. Table 3 displays numerical findings from this mathematical model, which have been validated against the published results of Ijaz and Nadeem [40]. This table demonstrates that the accepted FTCS code agrees very closely with the work of Ijaz and Nadeem [40].

Table 3. Comparison of present code (FTCS) with Ijaz and Nadeem [40] when $t = 1.2$, $\delta^* = 0.01$, $z = 1.5$ & $\phi = 0.0$.

Radius (x)	Ijaz and Nadeem [40]	Present Results
0.1	0.00	0.00
0.2	0.0317	0.0318
0.3	0.0418	0.0422
0.4	0.0420	0.0426
0.5	0.0366	0.0364
0.6	0.0283	0.0281
0.7	0.0191	0.0195
0.8	0.0109	0.0107
0.9	0.0052	0.0049
1.0	0.0039	0.0037

5. Response Surface Methodology (RSM)

The response surface approach is the most effective statistical model for examining and enhancing the impact of key flow field variables on the rate of heat transfer. The face-centered central composite design (CCD) is a prominent technique in the realm of response surface methodology (RSM), originally introduced by Box and Wilson [41]. The present investigation focuses on the impact of effective parameters E_1, M_a, and N_R response variables, specifically the heat transfer rate (Nu). Table 4 illustrates the range of chosen influential variables and their corresponding numerical values. The subsequent statement presents the fundamental structure of correlations established between effective parameters and response variables utilizing a three-level, three-factor face-centered central composite design–response surface methodology.

Table 4. Key parameters, their symbols, and their levels for RSM.

Key Factors	Symbols	Levels		
		−1 (Low)	**0 (Medium)**	**1 (High)**
E_1	X_1	0	0.15	0.3
M_a	X_2	2	3	4
N_R	X_3	1	2	3

There exist three distinct variables denoted as X_1, X_2, and X_3. It is noteworthy that the experimental design utilized in this study comprises 20 sets of runs, with the respective combinations for each set being presented in Table 5. Moreover, this arrangement considers six points along the axial plane, ten points along the factorial plane, and six points at the center.

Table 5. Heat transfer rate experimental design and outcomes.

Order	Code Values			Real Values			Nu
	X_1	X_2	X_3	E_1	M_a	N_R	
1	−1	−1	−1	0	2	1	0.9976488691
2	1	−1	−1	0.2	2	1	0.9658803418
3	−1	1	−1	0	4	1	1.070878107
4	1	1	−1	0.2	4	1	1.048387126
5	−1	−1	1	0	2	3	0.6579508725
6	1	−1	1	0.2	2	3	0.6724322264
7	−1	1	1	0	4	3	0.6931118918
8	1	1	1	0.2	4	3	0.7374430155
9	−1	0	0	0	3	2	0.8565814294
10	1	0	0	0.2	3	2	0.8550546489
11	0	−1	0	0.1	2	2	0.8365974307
12	0	1	0	0.1	4	2	0.9595528161
13	0	0	−1	0.1	3	1	1.113936950
14	0	0	1	0.1	3	3	0.7584564621
15	0	0	0	0.1	3	2	0.9115447848
16	0	0	0	0.1	3	2	0.9115447848
17	0	0	0	0.1	3	2	0.9115447848
18	0	0	0	0.1	3	2	0.9115447848
19	0	0	0	0.1	3	2	0.9115447848
20	0	0	0	0.1	3	2	0.9115447848

5.1. Accuracy of the Mode

The evaluation of the precision of this experimental framework is conducted through the utilization of the ANOVA analysis and residual plots. The ANOVA test results for the scenario in close proximity to the wall are presented in Table 6. The significance of independent parameters is influenced by linear, square, and two-way interactions. The significance of independent parameter importance can be effectively determined through the utilization of the *p*-value. When the *p*-value is less than 0.05, certain factors are observed to have a significant impact on the rate of heat transfer. Through the assessment of F and *p* values, it is possible to ascertain the variance of the data and to establish the statistical significance of the regression model. Model terms are considered statistically significant and are included in the analysis if their F value exceeds 1 and their *p* value is less than 0.05. Conversely, if these criteria are not met, the model terms are deemed insignificant and are not taken into consideration. Consequently, the quadratic element of variable M_a, along with the interaction factors of variables E_1, M_a, and N_R, have been removed from the Nu* model. Furthermore, the statistical estimators pertaining to the reduced models for Nu* have been demonstrated to retain their significance and are displayed in Table 6. The model for Nu* can be derived by solely considering the significant regression coefficients presented in Table 6.

Table 6. Sensitivity values at all levels of the key factors.

Source	DF	Adj SS	Adj MS	F-Value	*p*-Value
Model	9	0.316308	0.035145	200.20	0.000
Linear	3	0.295701	0.098567	561.47	0.000
E_1	1	0.000001	0.000001	0.01	0.944
M_a	1	0.014354	0.014354	81.76	0.000
N_R	1	0.281346	0.281346	1602.65	0.000
Square	3	0.018432	0.006144	35.00	0.000
E_1 * E_1	1	0.009874	0.009874	56.25	0.000
M_a * M_a	1	0.000858	0.000858	4.89	0.051
N_R * N_R	1	0.001151	0.001151	6.56	0.028
2-Way Interaction	3	0.002175	0.000725	4.13	0.038
E_1 * M_a	1	0.000191	0.000191	1.09	0.321
E_1 * N_R	1	0.001598	0.001598	9.10	0.013
Ma * N_R	1	0.000386	0.000386	2.20	0.169
Error	10	0.001756	0.000176		
Lack-of-Fit	5	0.001756	0.000351	*	*
Pure Error	5	0.000000	0.000000		
Total	19	0.318064			

The uncoded coefficients:

Regression Equation in Uncoded Units

$$\begin{aligned}
\mathrm{Nu} &= 0.9989 + 0.772\ \mathrm{E_1} + 0.1529\ \mathrm{M_a} - 0.2429\ \mathrm{N_R} \\
&- 5.992\ \mathrm{E}_1^2 - 0.01766\ \mathrm{M}_a^2 + 0.02046\ \mathrm{N}_R^2 \\
&+ 0.0489\ \mathrm{E_1} \times \mathrm{M_a} + 0.1413\ \mathrm{E_1} \times \mathrm{N_R} - 0.00695\ \mathrm{M_a} \times \mathrm{N_R}
\end{aligned}$$

The validation of the model's accuracy is achieved by employing residual plots for the responses Nu, as illustrated in Figure 2. The normal probability plot exhibits a linear trend where all data points are aligned. The presented histogram illustrates that the data exhibit a degree of symmetry and minimal skewness. This illustrates that the acquired data are representative. The residual versus fitted plot indicates that the maximum residual for Nu is approximately 0.0623. Furthermore, the value of S is 0.0132495, the coefficient of determination (R2) is 99.45%, the adjusted R2 is 99.95%, and the predicted R2 (R2 (Pred)) is 95.52%, indicating a high degree of correlation and a well-fitted model. The aforementioned particulars provide evidence for the assertion that the chosen model is dependable and appropriately fitting.

5.2. Response Surface Analysis

Figure 3 discovers the silhouette plots projected to explore the influences of operative factors (E_1, M_a, and N_R) on the responses Nu. Figure 3a–c depict the effect of Figure 3a interaction M_a with E_1 with hold N_R, Figure 3b interaction M_a with M_a with hold E_1, and Figure 3c interaction N_R with E_1 with hold M_a on Nu. It is notable that at all levels, the interaction of two factors is carried out, and the medium value of the third parameter is fixed as a hold value. The heat transfer rate is increased by the lower M_a and E_1 values. In the cases of M_a and E_1, the similar nature is shown. As N_R and E_1 are increased, the rate of heat transfer increases. Figure 3a reveals the influence of M_a and E_1 on the heat transfer rate. It is observed that lower levels of M_a (2–3) and all levels of E_1 result in a reduction in the heat transfer rate. However, increasing the magnetic field from 3.5 to 5 leads to a significant enhancement in the heat transfer rate for all levels of E_1. Moreover, analysis of Figure 3b,c reveals that varying the levels of N_R consistently leads to a significant decrease in the heat transfer rate. However, an increase in M_a within the range of 3–4 and E_1 within the range of 0.05–0.1 effectively enhances the heat transfer rate, particularly when the level of N_R is relatively low. The comprehensive findings from these figures indicate a clear correlation between the heat transfer rate of the hybrid nanofluid and the levels of thermal radiation and magnetic field. Specifically, a lower level of thermal radiation coupled with a higher level of magnetic field exhibits a pronounced enhancement in the heat transfer rate.

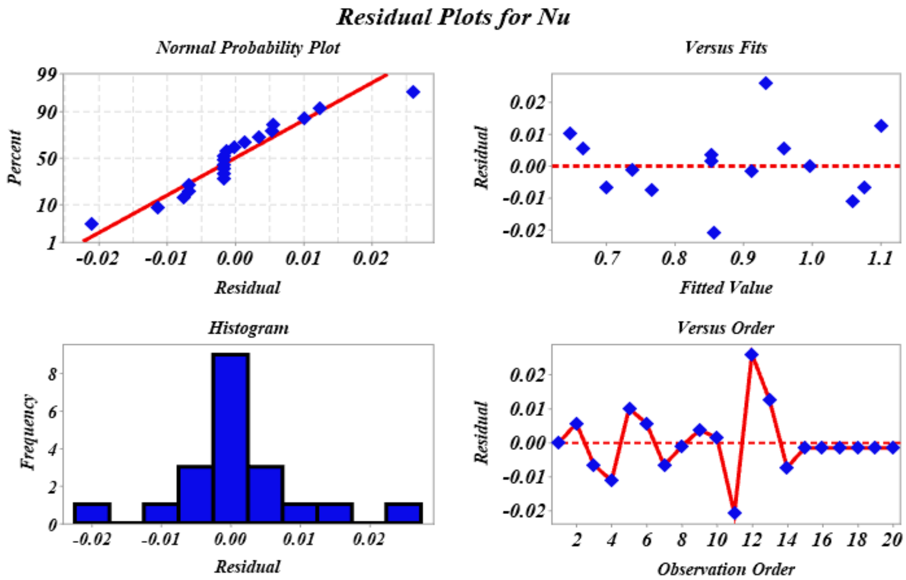

Figure 2. Residual plots for Nu.

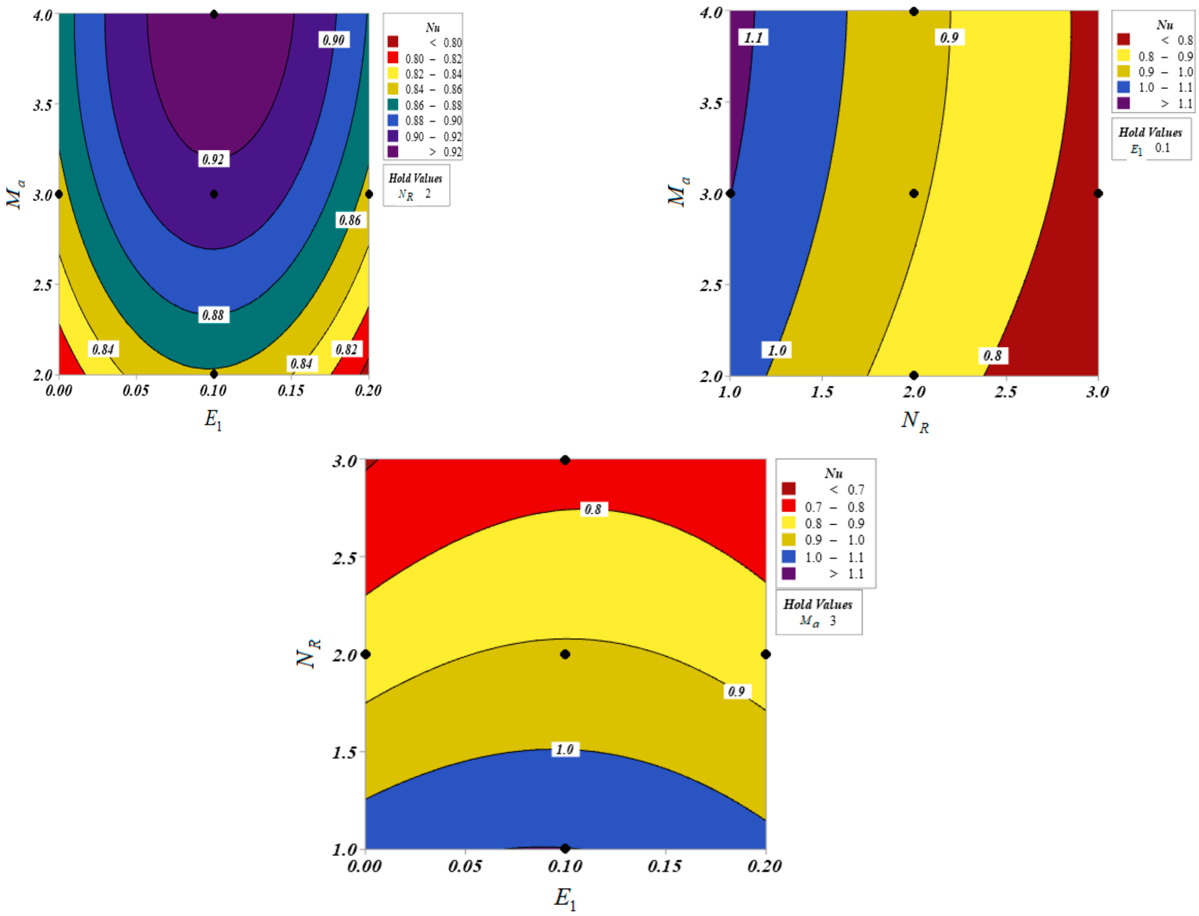

Figure 3. Contour plot for the various interactive parameters on the Nusselt number.

5.3. Sensitivity Analysis

This section employs independent parameters to ascertain the level of sensitivity of the heat transfer rate. The utilization of sensitivity functions involves the evaluation of changes in responses (Nu) in relation to the variables, namely E_1, M_a, and N_R, which are derived from the regression equation. These sensitivity functions are employed to determine any progression or regression in the responses.

$$\frac{\partial Nu}{\partial \mathrm{E_1}} = 0.772 - 11.984X_1 + 0.0489X_2 + 0.1413X_3,$$
$$\frac{\partial Nu}{\partial \mathrm{M_a}} = 0.1529 + 0.0489X_1 - 0.03532X_2 - 0.00695X_3,$$
$$\frac{\partial Nu}{\partial \mathrm{N_R}} = -\ 0.2429 + 0.1413X_1 -\ 0.00695X_2 + 0.04092X_3.$$

It is critical to note that Table 7 displays all values of the other two parameters, and that the sensitivity is calculated for the medium value of X_1 alone. To investigate the sensitivity of independent factors, Figure 4 is shown. It is obvious that M_a is the positive side and that N_R and E_1 have a negative sensitivity.

Table 7. Response sensitivity at the medium value of $\mathrm{E_1}$.

Order	X_1	X_2	X_3	$\frac{\partial Nu_{avg}}{\partial X_1}$	$\frac{\partial Nu_{avg}}{\partial X_2}$	$\frac{\partial Nu_{avg}}{\partial X_3}$
1	0	−1	−1	−0.0155	0.08020	−0.2028
2	0	−1	0	0.2976	0.07325	−0.16209
3	0	−1	1	0.6107	0.06630	−0.12180
4	0	0	−1	0.0334	0.04488	−0.20933
5	0	0	0	0.3465	0.03793	−0.16904
6	0	0	1	0.6596	0.03098	−0.12875
7	0	1	−1	0.0823	0.00956	−0.21628
8	0	1	0	0.3954	0.00261	−0.17599
9	0	1	1	0.7085	−0.00434	−0.13570

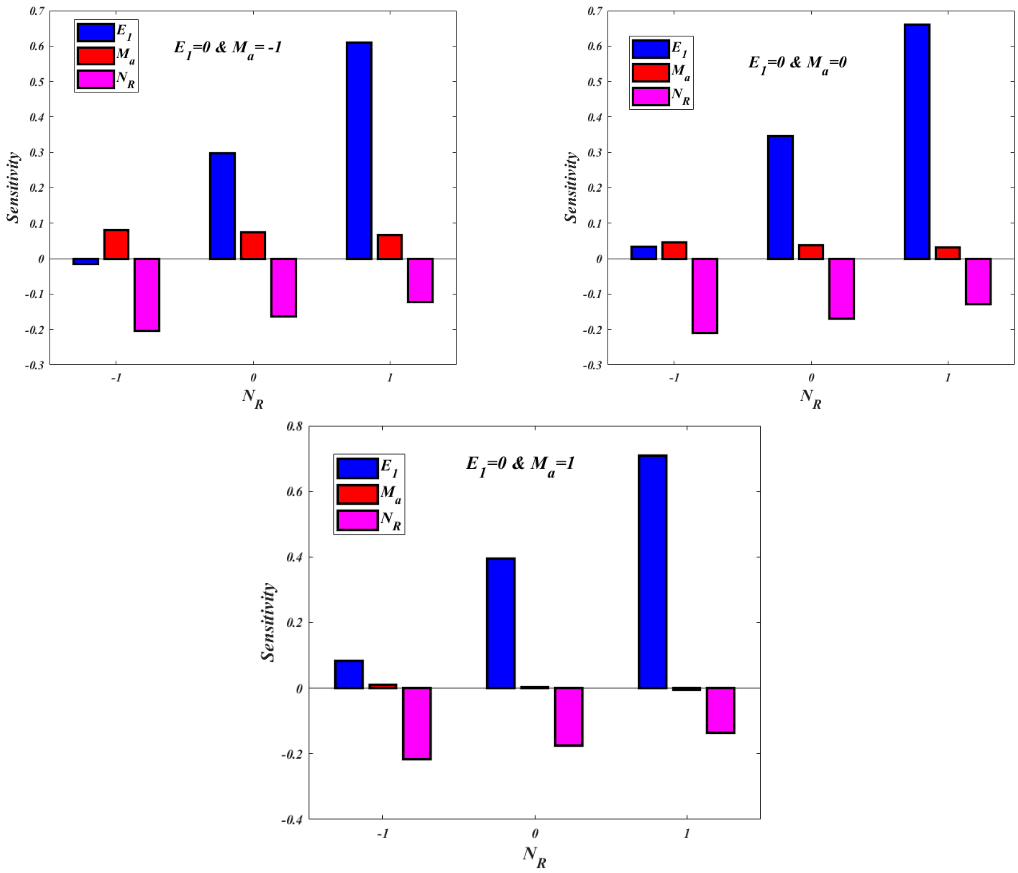

Figure 4. Sensitivity of operational parameters.

6. Results and Discussion

This section is intended to demonstrate the heat transfer behavior of EMHD blood-based silver–titanium dioxide nanoparticles in a tilted cylindrical W-shape stenosis artery with the entropy generation analysis velocity, temperature, wall shear stress, flow rate, resistance to flow, and total entropy generation visualized and elaborately discussed. The moderate stenotic approximation was applied after the two-dimensional governing equations were translated and normalized using the relevant variables. The FTCS technique was used since the resulting dimensionless boundary value problem's substantially nonlinear nature called for a reliable numerical approach. Comparisons of Ag–TiO_2 hybrid nanofluid and Ag nanofluid in a tilted cylindrical W-shape stenosis are shown using solid and dotted lines, respectively. In accordance with Sharma et al. [25], Gandhi et al. [26], Tripathi et al. [27], and Basha et al. [28], the graphical outcomes were presented using a specific combination of parameters: $\mathrm{Pr} = 14,\ R_e = 2,\ E_1 = 0.1,\ z = 0.98,\ M_a = 1,\ B_1 = 1.41,$ $\phi_1 + \phi_2 = 0.05,\ w_s = 0.1,\ \delta^* = 0.1,\ c_1 = 1,\ d = 2,\ B_2 = 2,\ E_C = 1,\ N_R = 1,$ $Q = 0.2,\ \beta_0 = 0.5,$ and $t = 1.2$. The obtained data exhibit consistency between stenotic blood flows and nanoparticle drug delivery [42].

The velocity and temperature profiles that are dimensionless for different values of the electric field parameter (E_1) are illustrated in Figure 5a, showing that enhancing the performance leads to an elevation in the velocity profile for both Ag–TiO_2 hybrid nanofluid and Ag nanofluid. Increasing the electric field parameter E_1 leads to a noticeable increase in flow velocity. This can be attributed to the accelerating force induced by the electric field, which acts in the direction of the applied electric field. Consequently, the momentum boundary layer thickness expands, resulting in the acceleration of the fluid. The figure reveals that as the value of E_1 increases from 0 to 0.15, the blood velocity shows a significant rise of 26.83% in the hybrid nanofluid case, similar to a 26.53% increase observed in the silver nanofluid case. Figure 5b demonstrates the impact of the Hartmann number (M_a) on the velocity profile of Ag–TiO_2 hybrid nanofluids in the blood. It is observed that an increase in M_a (indicative of a stronger Lorentzian drag force) significantly hinders the blood flow in the core region, which is located near the artery's centerline. When $M_a = 0$, corresponding to a zero radial magnetic field, the blood behaves as a non-conducting fluid. When $M_a = 2$, both the magnetic and viscous hydrodynamic forces are equally influential. The presence of a stronger magnetic field effectively regulates and attenuates the blood flow, offering improved control in biomedical procedures through nonintrusive means, such as the application of an external magnetic field. This parameter also plays a crucial role in adjusting the fluid velocity. According to the figure, it is evident that an increase in the values of M_a from 2 to 5 leads to a significant reduction in blood velocity. In particular, the hybrid nanofluid case demonstrates a substantial decline of 64.19.83%, and a similar decrease of 64.14% is observed in the silver nanofluid case.

The visualization of the impact of Reynolds number (Re) on blood flow velocity and temperature profile is presented in Figure 6a,b. It is worth mentioning that the analysis pertains to extremely low Reynolds numbers, indicating laminar flow; consequently, the system is governed by viscous forces. The results of the computations indicate that an increase in the Reynolds number from 2 to 5 has resulted in a noteworthy decrease in velocity. Similarly, with an increase in Reynolds number, there is a corresponding decrease in temperature. Despite the fact that the Reynolds number (based on the vessel radius) causes an increase in inertial force, the primary impact is the deceleration of flow due to stenotic obstruction and nanoparticles. This results in a considerable impediment to the streaming blood. At higher Reynolds numbers, temperature suppression occurs and the profiles exhibit a decreasing gradient. The profiles become attached to the zero line, and subsequent temperature growth from the wall occurs over longer radial distances. It is observed that varying the Reynolds number from 2 to 5 results in a decrease in fluid velocity and temperature. Specifically, for hybrid nanofluids, there is a reduction of 15.72% in fluid velocity and 85.15% in temperature, whereas for silver nanofluids, the corresponding reductions are 17.51% and 85.82%, respectively.

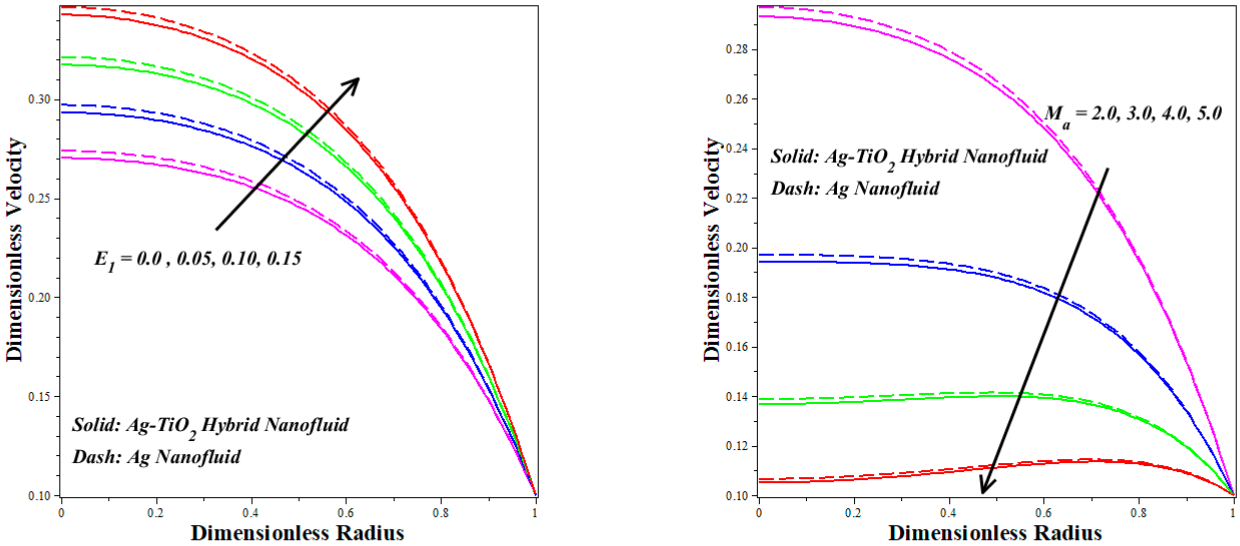

(**a**) (**b**)

Figure 5. Velocity for different values of (**a**) Electric field (E_1) and (**b**) Hartmann number (M_a) at $\mathrm{Pr} = 14,\ R_e = 2,\ z = 0.98,\ \delta^* = 0.1,\ \phi_1 + \phi_2 = 0.05,\ w_s = 0.1,\ E_C = 1,\ Q = 0.2,\ N_R = 1,\ t = 1.2$.

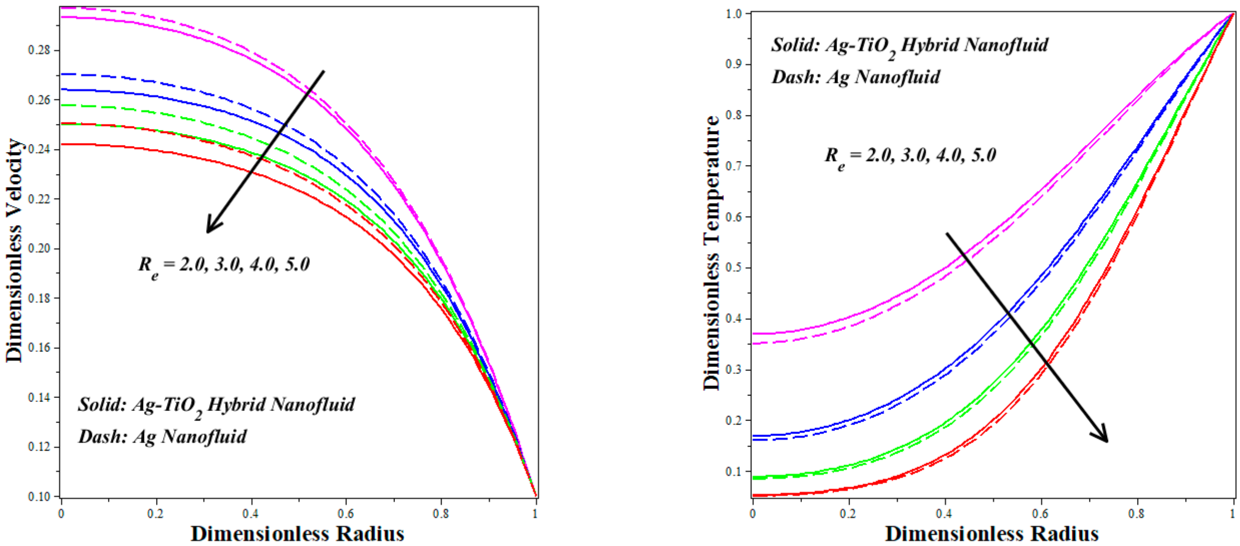

(**a**) (**b**)

Figure 6. (**a**) Velocity and (**b**) Temperature for different values of Reynolds number (R_e) at $\mathrm{Pr} = 14,\ M_a = 2,\ z = 0.98,\ E_1 = 0.1,\ \phi_1 + \phi_2 = 0.05,\ w_s = 0.1,\ E_C = 1,\ Q = 0.2,\ N_R = 1,\ t = 1.2$.

The velocity and temperature profiles' development is illustrated in Figure 7a,b concerning the variation in Ag–TiO_2 hybrid nanofluids and Ag nanofluids and wall slip velocity. The study indicates that an elevation in the wall slip parameter results in a corresponding augmentation of the blood flow velocity in the vicinity of the artery's centerline. The velocity profile of a blood nanofluid experiences an increase in the wall slip parameter, which can be attributed to a multitude of factors. These factors include heightened shear stress and turbulence in the vicinity of the boundary at elevated velocities, as well as the intricate interdependence between the fluid properties and boundary conditions. Figure 7b illustrates that as the slip parameter increases, there is a noticeable rise in acceleration temperature. The imposition of the slip parameter at the inner surface of the arterial wall serves as a boundary condition. The slip velocity's existence results in a momentum increase that aids the blood in the near-wall region and quickens blood flow. However, the impact diminishes as the radial distance from the arterial centerline increases. The variation of wall slip from 0 to 0.3 leads to an increase in both fluid velocity and temperature. In the case of hybrid nanofluids, the fluid velocity experiences a rise of 64.06%, whereas the temperature decreases by 84.34%. Similarly, for silver nanofluids, the corresponding enlargement is 65.41% in fluid velocity and 66.33% in temperature.

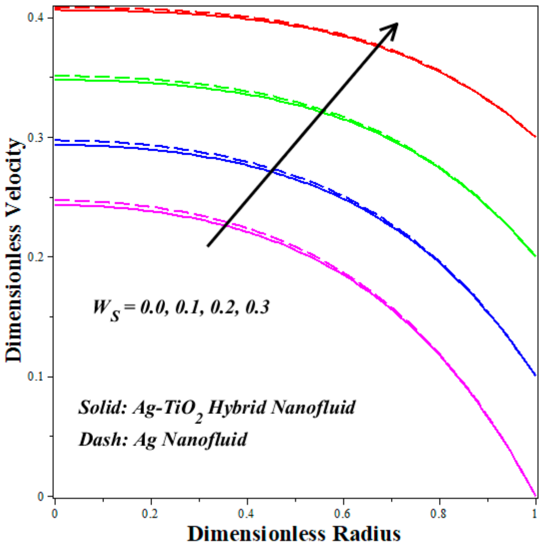

(**a**)

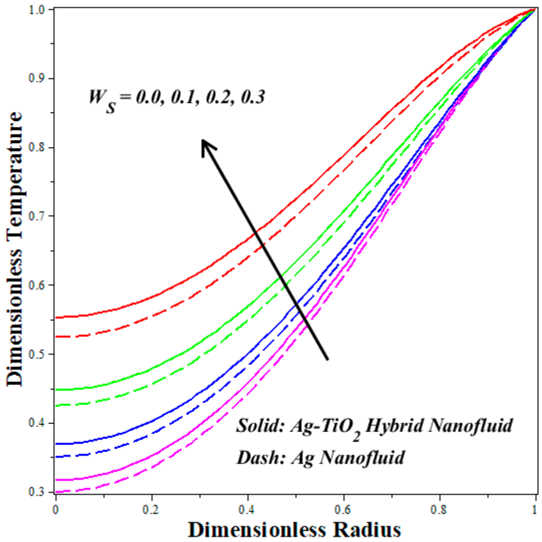

(**b**)

Figure 7. (**a**) Velocity and (**b**) Temperature for different values of wall slip parameter (w_s) at $\mathrm{Pr} = 14,\ M_a = 2,\ z = 0.98,\ E_1 = 0.1,\ \phi_1 + \phi_2 = 0.05,\ R_e = 2,\ E_C = 1,\ Q = 0.2,\ N_R = 1,\ t = 1.2$.

Figure 8a,b provide a graphic representation of how the Eckert number (Ec) affects the blood flow velocity and temperature profile. The research findings suggest that an increase in the Eckert number (Ec) leads to a proportional enhancement of the velocity of blood flow in the proximity of the centerline of the artery. The increase in the Eckert number (Ec) is responsible for the alteration of the velocity profile of a blood nanofluid, and this phenomenon can be attributed to various factors. Figure 8b illustrates the impact of Ec on the nondimensional temperature profile. The rise in the Ec value indicates a corresponding rise in the temperature distribution within the flow zone. This phenomenon is attributed to the accumulation of heat energy in the fluid due to frictional heating, leading to an increase in the temperature of the fluid (blood). When the Eckert number is varied from 0 to 1, both fluid velocity and temperature show a noticeable increase. The elevation in fluid velocity is 13.14% for hybrid nanofluids and 12.44% for silver nanofluids. Additionally, the temperature experiences a significant incline of 120.72% in the case of hybrid nanofluids, and a corresponding reduction of 130.53% is observed for silver nanofluids. The temperature profile is investigated by plotting Figure 9a,b to examine the impact of heat source parameter (Q) and thermal radiation (N_R) features. The diagram depicted in Figure 9a demonstrates the correlation between the heat source parameter and the temperature profile. The figure indicates that the temperature profile rate is augmented by the (Q) settings. The temperature distribution of a blood nanofluid, subject to a heat source, is contingent on the distinct characteristics of both the fluid and the source of heat. The fluid's behavior may be influenced by various factors, including the concentration and size distribution of the suspended particles, the thermal conductivity and heat capacity of the fluid, and the geometry and distribution of the heat. By varying Q from 0 to 0.6 and N_R from 0 to 3, a noticeable increase in temperature is observed. Specifically, for hybrid nanofluids, the temperature experiences a significant elevation of 8.17% for Q and 194.47% for N_R. Similarly, in the case of silver nanofluids, the corresponding enhancements in temperature are 9.09% for A1 and 205.42% for N_R source. The data presented in Figure 9b indicate that enhancing thermal radiation (N_R) has a positive correlation with the temperature profile. The temperature profile exhibits an upward trend as the values of Nr increase. This phenomenon occurs because of the Inverse relationship between the radiation parameter and thermal conductivity, indicating that the system dissipates more heat through radiation. Radiation acts as a source of heat within the bloodstream, and higher radiation levels result in an elevation of temperature. When nanoparticles, such as gold and alumina, interact with light of the appropriate wavelength, the free electrons within them undergo oscillations. The heat generated by these oscillations spreads to the surrounding environment, leading to the destruction of malignant cells. This discovery holds significant potential in the field of thermal therapy, offering numerous applications for targeted cancer treatment. Figure 10 shows the wall shear stress profiles for a variety of factors, including the thermal radiation (N_R), electric field (E_1), amplitude of body acceleration (B_2), and Eckert number (E_c). Figure 10a illustrates the impact of (N_R) on wall shear stress. As the (N_R) values increase, there is an inclination in the wall shear stress profiles. The phenomenon of thermal-radiation-induced temperature rise is limited to a specific area, and it may result in an opposing outcome, whereby a localized temperature increase can trigger a corresponding rise in the viscosity of the blood in that particular region. The augmentation in viscosity may lead to a rise in the wall shear stress due to the amplified frictional drag on the surface. Figure 10b demonstrates the influence of the electric field (E_1) on the profiles of wall shear stress. As the (E_1) values increase, there is an inclination in the wall shear stress profiles. For different values of the dimensionless amplitude of the body acceleration, Figure 10c shows the dimensionless steady state period at which the minimum blood flow is attained in the wall shear stress profiles. The viscous drag force that a body experiences when moving in a fluid is what causes the amplitude of body acceleration (B_2) to decrease as wall shear stress increases. Figure 10d shows that the wall shear stress enlargements as the Eckert number (E_c) increases. The variations in E_1, N_R, and E_c have a promoting effect on wall shear stress, leading to values of 41.02%, 14.33%, and 10.05% for the hybrid nanofluid case and 38.45%, 14.29%, and 9.74% for the unitary nanofluid case. On the other hand, the effect of B_2 causes a reduction in wall shear stress, with values of 18.15% observed for the hybrid nanofluid and 15.47% for the unitary nanofluid. From these figures, it is evident that the unitary nanoparticles yield a significantly higher wall shear stress compared to the hybrid nanoparticles. This can be attributed to the dominant fluid velocity behavior exhibited by the silver nanoparticles in the W-shaped stenotic artery.

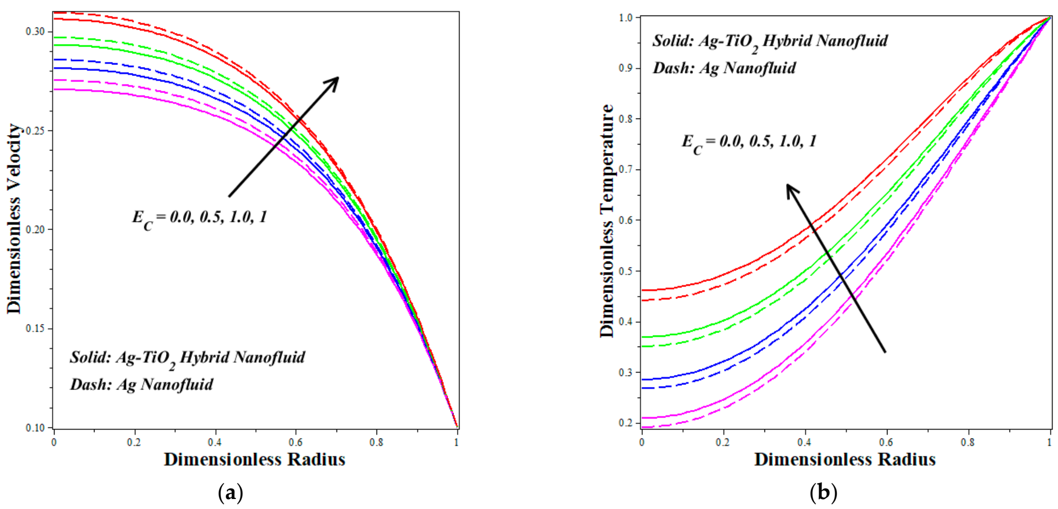

Figure 8. (**a**) Velocity and (**b**) Temperature for different values of Eckert number (E_c) at $\Pr = 14,\ M_a = 2,\ z = 0.98,\ E_1 = 0.1,\ \phi_1 + \phi_2 = 0.05,\ w_s = 0.1,\ Q = 0.2,\ N_R = 1,\ t = 1.2$.

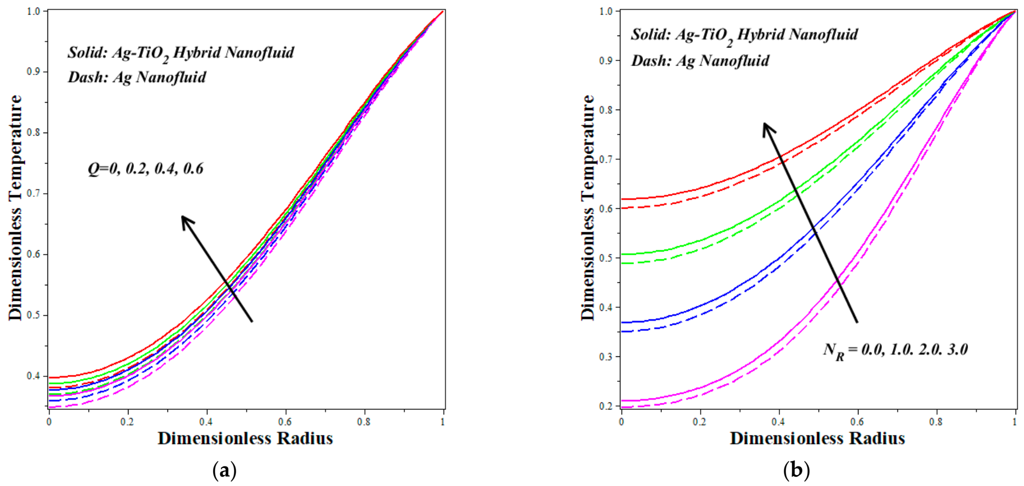

Figure 9. Temperature for different values of (**a**) heat source parameter (Q) (**b**) thermal radiation (N_R) at $\mathrm{Pr} = 14,\ M_a = 2,\ z = 0.98,\ E_1 = 0.1,\ \phi_1 + \phi_2 = 0.05,\ w_s = 0.1,\ B_1 = 1.41,\ B_2 = 2,\ E_C = 1,\ t = 1.2$.

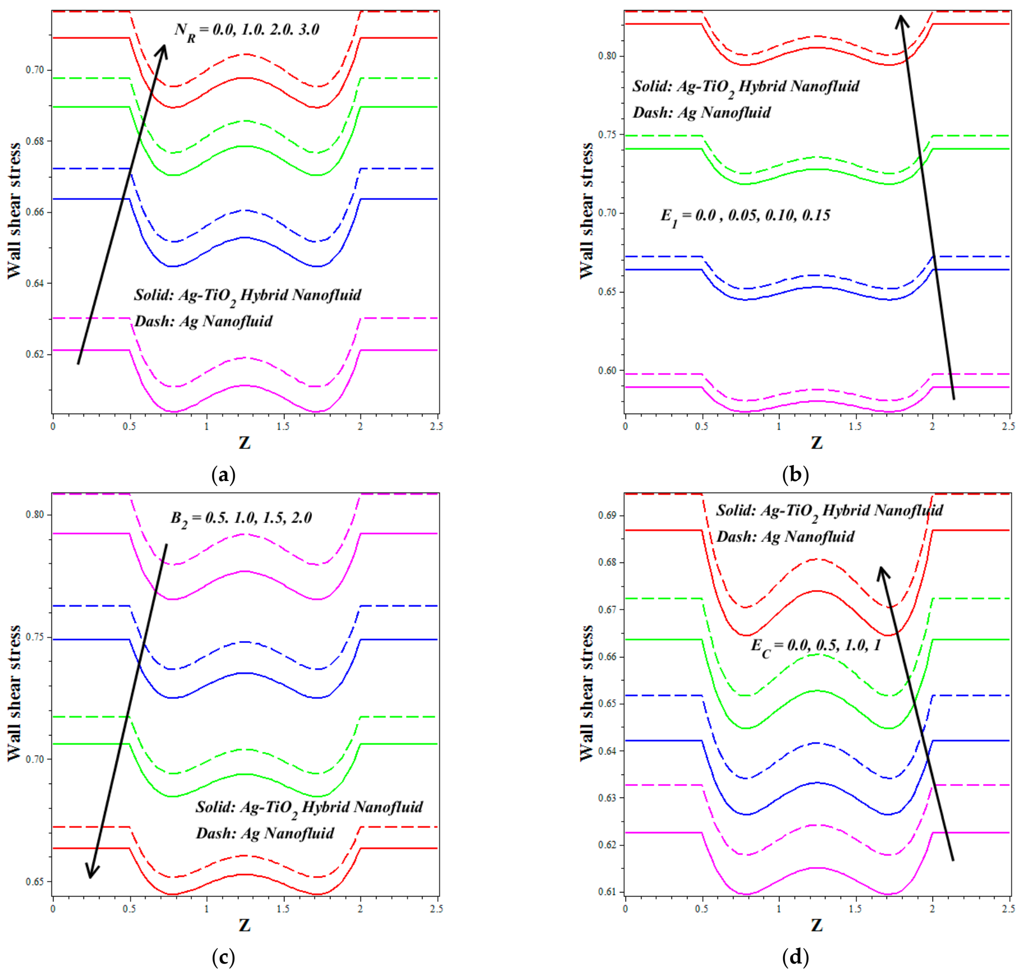

Figure 10. Wall shear stress for different values of (**a**) thermal radiation (N_R) (**b**) electric field (E_1), (**c**) amplitude of body acceleration (B_2) and (**d**) Eckert number (E_c) at $\mathrm{Pr} = 14,\ M_a = 2,\ z = 0.98,\ \phi_1 + \phi_2 = 0.05,\ w_s = 0.1,\ B_1 = 1.41,\ Q = 0.2,\ t = 1.2$.

The effects of different wall slip velocity (W_s) and Womersley numbers (Λ) on the volumetric flow rate are shown in Figure 11a,b. The Womersley numbers on the volumetric flow rate in the situations of Ag–TiO_2 hybrid nanofluids and Ag nanofluids show the opposite nature, and this quantity likewise greatly rises for the larger values of the wall slip velocity. The slip velocity at the wall lowers the effective fluid viscosity and causes a thinner boundary layer, which, in turn, causes the flow rate to drop for higher values of the wall slip velocities. In the hybrid nanofluid case, the variation of slip velocity leads to an increase in flow rate, with a value of 132.55. Similarly, in the unitary nanofluid case, the flow rate is boosted with a value of 124.10. Additionally, the effect of Womersley numbers results in a decrease of 15.92 for the hybrid nanofluid and 14.07 for the unitary nanofluid. The effects of different Hartmann numbers (M_a) and Reynolds numbers (R_e) on the resistance to flow are shown in Figure 12a,b. The diagram depicted in Figure 12a demonstrates the correlation between the Hartmann number (M_a) and the resistance to flow. The figure indicates that the resistance to flow profile rate is augmented by the (M_a) situations in both the Ag–TiO_2 hybrid nanofluids and Ag nanofluids. Figure 12b also has the same nature for the higher values of the Reynolds number (R_e) in the resistance to flow. The impacts of M_a and R_e on hybrid nanofluids leads to significant enhancements in resistance impedance, with values of 89.58% and 17.48%, respectively. In addition, for the unitary nanofluid, the enhancements are observed as 108.05% and 15.83%, respectively.

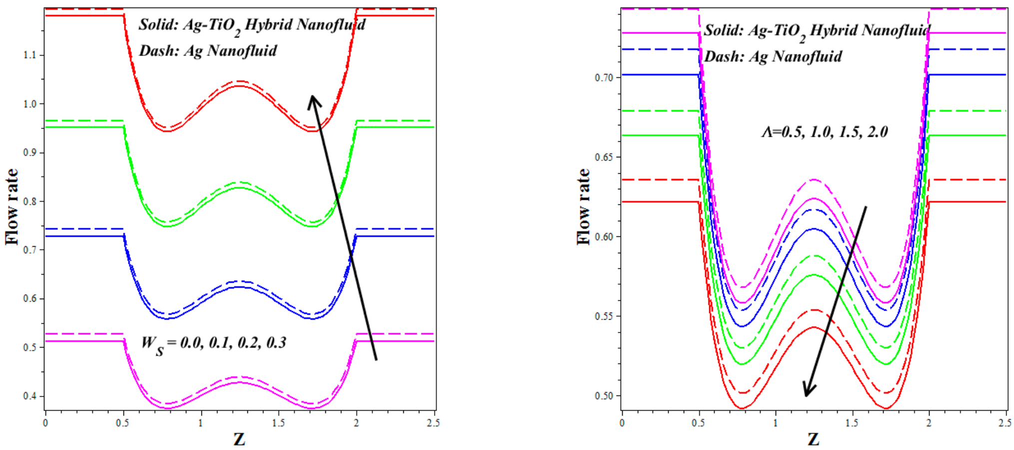

(a) (b)

Figure 11. Flow rate for different values of (**a**) wall slip velocity (W_s) (**b**) Womersley number (Λ) at $\mathrm{Pr} = 14,\ M_a = 2,\ z = 0.98,\ E_1 = 0.1,\ \phi_1 + \phi_2 = 0.05,\ N_R = 1,\ B_1 = 1.41,\ B_2 = 2,\ E_C = 1,\ t = 1.2.$

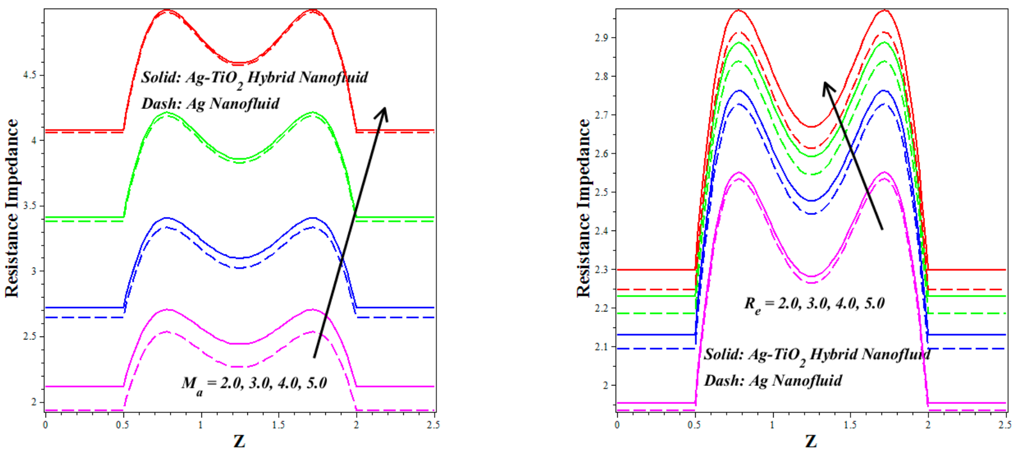

(a) (b)

Figure 12. Resistance to flow for different values of (**a**) Hartmann number (M_a) (**b**) Reynolds number (R_e) at $\mathrm{Pr} = 14,\ \Lambda = 1.0,\ z = 0.98,\ E_1 = 0.1,\ w_s = 0.1,\ \phi_1 + \phi_2 = 0.05,\ N_R = 1,\ B_1 = 1.41,\ B_2 = 2,\ E_C = 1,\ t = 1.2.$

Figure 13a–f show that the total entropy production has been studied by looking at the thermal radiation (N_R), wall slip velocity (W_s), electric field (E_1), Brickman number (Br), amplitude of body acceleration (B_2), and temperature difference (Ω) through numerical integration. Figure 13a shows that increasing thermal radiation (N_R) tend to enhance the generation of entropy. The phenomenon of entropy generation is observed to be directly proportional to the radiation parameter, as the latter leads to an augmented radiative heat transfer between the system and its surroundings. This, in turn, causes a significant rise in the temperature differential, thereby resulting in a greater degree of irreversibility. The inverse relationship between the entropy generation profile and wall slip velocity (W_s) is depicted in Figure 13b. The increase in wall slip velocity results in a decrease in entropy generation due to the reduction in frictional forces and subsequent decrease in the rate of irreversibility within the boundary layer. The tendency for increasing entropy production to occur when the electric field (E_1) is raised is seen in Figure 13c. The phenomenon of entropy generation exhibits a positive correlation with elevated levels of electric field due to the generation of joule heating by the electric field. This, in turn, leads to an increase in temperature gradient and, consequently, a higher rate of irreversibility. It is observed that higher values of the Brickman number (Br) to the entropy generation is initially increasing and reducing, which is shown in Figure 13d. Figure 13e shows that increasing amplitude of body acceleration (B_2) tends to enhance the generation of entropy. The amplitude of body acceleration has a direct impact on entropy generation, as higher values of acceleration result in the production of additional mechanical work. This, in turn, leads to a greater rate of irreversibility and a subsequent increase in the generation of entropy. It is observed that higher values of the temperature difference (Ω) to the entropy generation is initially decreasing and rising, which is shown in Figure 13f. Increasing the values of Ω in the system leads to a reduction in joule heating irreversibility, hybrid nanofluid friction irreversibility, and heat transfer irreversibility. As a result, the total entropy generation decreases near the wall. However, the dominant influence of resistive force and electric field on the behavior of Ω causes an increase in total entropy production near the top wall. The figures demonstrate a noticeable disparity in total entropy generation between the top and bottom walls. Specifically, the hybrid nanofluid case shows an increase of approximately 3019.67% at the top wall, and the unitary nanofluid case exhibits an increase of approximately 3242.86%.

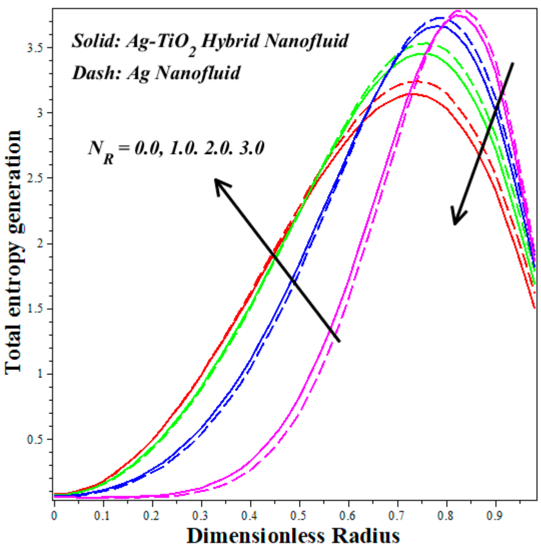

(**a**)

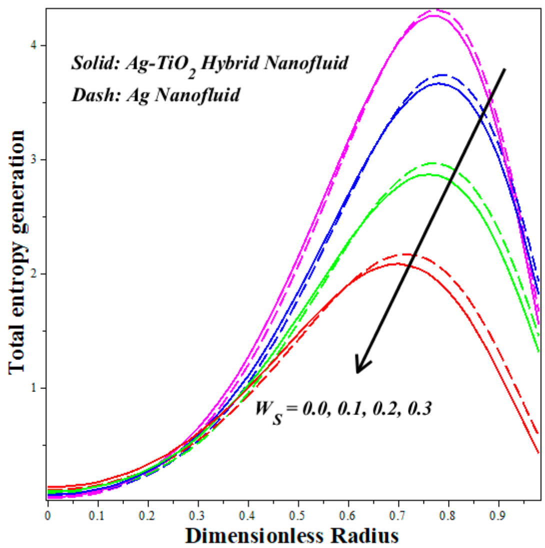

(**b**)

Figure 13. *Cont*.

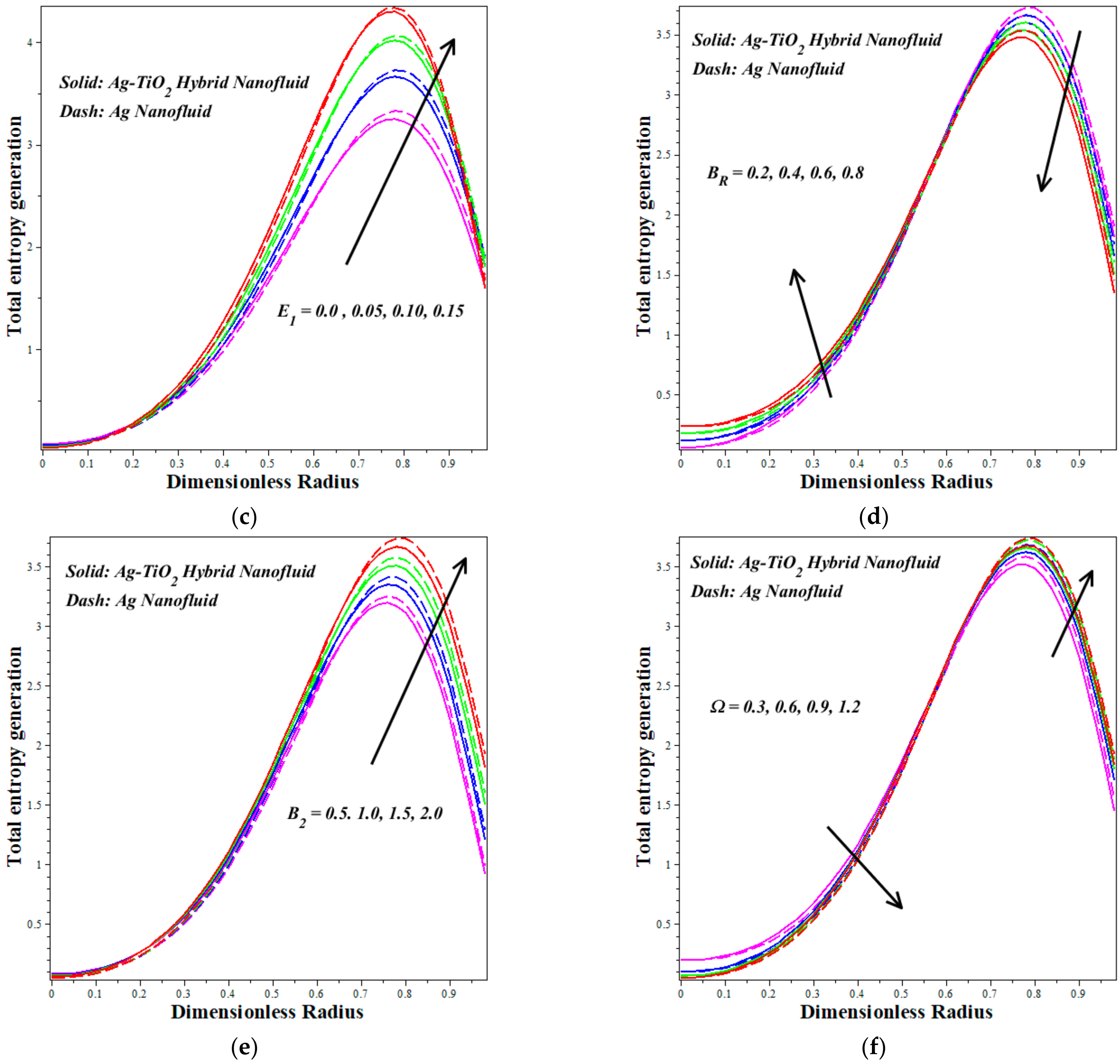

Figure 13. Total entropy generation for different values of (**a**) thermal radiation (N_R), (**b**) wall slip velocity (W_s), (**c**) electric field (E_1), (**d**) Brickman number (Br), (**e**) amplitude of body acceleratio (B_2) and (**f**) temperature difference (Ω) at $\mathrm{Pr} = 14,\ \Lambda = 1.0,\ z = 0.98,\ \delta^* = 0.1,\ d = 2,\ \phi_1 + \phi_2 = 0.05,$ $N_R = 1,\ B_1 = 1.41,\ E_C = 1,\ t = 1.2.$

7. Conclusions

This section is intended to demonstrate heat transfer behavior of EMHD blood-based silver–titanium dioxide nanoparticles in a tilted cylindrical W-shape symmetric stenosis artery with entropy generation analysis. The study draws inspiration from nano-drug delivery applications in magnetically assisted pharmacological fluid dynamics for the treatment of arterial diseases. The study incorporates the phenomena of wall slip and heat generation. The Reynolds exponential model is used in the formulation to replicate the temperature dependence of blood fluid viscosity. In order to accurately model realistic flow scenarios, it is necessary to incorporate the unsteady component of pulsatile pressure gradient. The present study involves the assessment of key hemodynamic parameters, including velocity, temperature, wall shear stress, and flow rate, in the stenotic region. This is achieved through the solution of transformed dimensionless conservation equations, subject to appropriate physiological initial and boundary conditions, using the FTCS (forward time centered space) finite difference method. The numerical code is validated through a comparison with previous hemodynamic studies that were nonmagnetic and had constant viscosity. The primary outcomes of the current calculations can be succinctly summarized as follows:

- ➢ When an external electric field is applied radially, it leads to a significant promotion of the axial velocity. Furthermore, a noteworthy decrease in blood velocity is observed with magnetic field in both hybrid and unitary blood nanofluids.
- ➢ By varying the Reynolds number within the range of 2 to 5, it is observed that both blood nanofluid cases experience a deceleration in axial velocity and a reduction in temperature magnitudes. The presence of hybrid nanoparticles in the blood results in a relatively smaller decrease in axial velocity compared to unitary nanoparticles.
- ➢ As the Eckert number increases, the nondimensional temperature profiles rise due to the crisscross movement of particles, resulting in collisions within the fluid. These collisions generate additional heat, contributing to the elevated temperature magnitudes.
- ➢ With increasing values of radiation, electric field, and Eckert number, the magnitudes of wall shear stress experience significant growth. Conversely, the wall shear stress values decrease as the body acceleration amplitude increases.
- ➢ By increasing the thermal radiation, the heat transfer rate of a hybrid nanofluid is reduced. Conversely, strengthening the magnetic field promotes the heat transfer rate. The interaction between these parameters reveals that a combination of lower radiation and a higher magnetic field leads to an elevated heat transfer rate.
- ➢ It is observed that the total entropy generation is higher at the top wall compared to the lower wall. Furthermore, hybrid nanofluids show a slightly increased total entropy generation away from the wall, while unitary nanofluids exhibit a significant rise in total entropy generation once they cross over from the center of the artery.
- ➢ By employing response surface methodology, it is revealed that combining a higher level of magnetic field with a lower level of thermal radiation results in a notable enhancement in the heat transfer rate.
- ➢ The statistical test results show that the present model achieves an improved heat transfer rate of 1.1289 when the parameters $E_1 = 0.1$, $N_R = 1$, and $M_a = 4$ are fixed. Conversely, a lower heat transfer rate of 0.6479 is obtained when $E_1 = 0.2$, $N_R = 3$, and $M_a = 2$.

Author Contributions: Conceptualization: E.A.A. and N.A.A.; methodology, A.S.A., M.E.E. and M.Z.; formal analyses: Y.Y.A., B.O.E.-B. and N.A.A.; data curation: A.S., E.A.A., F.A. and N.A.A.; investigation: A.S.A., F.A. and A.S.; writing—original draft: A.S.A., A.S. and F.A.; resources: M.E.E., M.Z. and B.O.E.-B.; supervision: N.A.A.,F.A., E.A.A. and B.O.E.-B.; project administration: E.A.A., A.S. and N.A.A.; review and editing: N.A.A.,M.E.E., M.Z., Y.Y.A. and N.A.A.; funding, E.A.A., N.A.A., M.E.E., M.Z. and Y.Y.A. All authors have read and agreed to the published version of the manuscript.

Funding: Deanship of Scientific Research at University of Tabuk, Tabuk, Saudi Arabia, for funding the project under the Project No. 0208-1443-S.

Institutional Review Board Statement: Not Applicable.

Informed Consent Statement: Not Applicable.

Data Availability Statement: Not Applicable.

Acknowledgments: The authors extend their appreciation to the Deanship of Scientific Research at University of Tabuk for funding the project under the project number 0208-1443-S.

Conflicts of Interest: We are reporting that we have no potential conflict of interest with any other author.

Nomenclature

$\overline{u}, \overline{v}$	Velocity components
$\overline{z}$	Axial coordinate
R_0	Radius of the healthy artery
$\overline{d}$	Distance from the origin of the stenosis
l_0	Total length of the stenosis artery
Q_0	Constant heat source
B_0	Uniform magnetic field
t	time
p	Pressure
r	radial coordinate
T	Temperature
C_{hnf}	Thermal expansion
g	Gravitational acceleration
$(Cp)_{hnf}$	Specific heat capacity
U_0	Reference velocity
M_a	Hartmann number
G_r	Grashof number
R_e	Reynolds number
E_c	Eckert number
T_w	Wall temperature
N_R	Thermal radiation
P_r	Prandtl number
A_0	Average pressure gradient
A_1	Average pulsatile amplitude
c_1, c_2	Body force
B_2	Body acceleration amplitude
Nu	Nusselt number
Q_F	Volumetric flow rate
N_g	Dimensionless entropy generation
B_r	Brickman number
Greek Symbols	
α	Angle
β_0	Viscosity constant
δ	Stenosis height parameter
θ	Dimensionless temperature
Λ	Womersley number
κ	Lead angle to the heartbeat
σ_{hnf}	Electrical conductivity
ρ_{hnf}	Density
ε	Vessel aspect ratio
k_{hnf}	Thermal conductivity
μ_{hnf}	Dynamic viscosity
τ_s	Wall shear stress
λ	Resistance impedance
Ω	Temperature difference
Subscripts	
hnf	Hybrid nanofluid
nf	Nanofluid

References

1. Atashafrooz, M.; Sajjadi, H.; Delouei, A.A. Simulation of combined convective-radiative heat transfer of hybrid nanofluid flow inside an open trapezoidal enclosure considering the magnetic force impacts. *J. Magn. Magn. Mater.* **2023**, *567*, 170354. [CrossRef]
2. Patil, P.; Kulkarni, M. Analysis of MHD mixed convection in a Ag-Tio2 hybrid nanofluid past a slender cylinder. *Chin. J. Phys.* **2021**, *73*, 406–419. [CrossRef]
3. Patil, P.; Benawadi, S.; Shanker, B. Influence of mixed convection nanofluid flow over a rotating sphere in the presence of diffusion of liquid hydrogen and ammonia. *Math. Comput. Simul.* **2021**, *194*, 764–781. [CrossRef]

4. Patil, P.; Shankar, H. Heat transfer attributes of Al_2O_3-Fe_3O_4/H_2O hybrid nanofluid flow over a yawed cylinder. *Propuls. Power Res.* **2022**, *11*, 416–429. [CrossRef]
5. Patil, P.M.; Goudar, B. Time-dependent mixed convection flow of Ag–MgO/water hybrid nanofluid over a moving vertical cone with rough surface. *J. Therm. Anal. Calorim.* **2022**, *147*, 10693–10705. [CrossRef]
6. Patil, P.M.; Goudar, B. Single and multiple walled CNTs-TiO_2 ternary hybrid nanofluid flow of Williamson fluid in an unsteady combined convective regime:An entropy analysis. *Numer. Heat Transf. Part A Appl.* **2023**. [CrossRef]
7. Mandal, G.; Pal, D. Dual solutions of radiative Ag-Mos_2/water hybrid nanofluid flow with vriable viscosity and variable thermal conductivity along an exponentially shrinking permeable Riga surface: Stability and entropy generation analysis. *Int. J. Model. Simul.* **2023**. [CrossRef]
8. Mandal, G.; Pal, D. Estimation of entropy generation and heat transfer of magnetohydrodynamic quadratic radiative Darcy-Forchheimer cross hybrid nanofluid (GO+Ag/kerosene oil) over a stretching sheet. *Numer. Heat Transf. Part A Appl.* **2023**. [CrossRef]
9. Mandal, G. Entropy Analysis on Magneto-Convective and Chemically Reactive Nanofluids Flow Over a Stretching Cylinder in the Presence of Variable Thermal Conductivity and Variable Diffusity. *J. Nanofluids* **2023**, *12*, 819–831. [CrossRef]
10. Halilu, A.; Umar, A.A.; Balarabe, Y.U.; Haniffa, M.A.C.M.; Munawar, K.; Sunku, K.; Sudarsanam, P. Advances in Single-Atom Catalysts for Lignin Conversion. In *ACS Symposium. Series*; American Chemical Society: Washington, DC, USA, 2020; pp. 93–125. [CrossRef]
11. Shahzad, F.; Jamshed, W.; Eid, M.R.; Ibrahim, R.W.; Aslam, F.; Isa, S.S.P.M.; Guedri, K. The effect of pressure gradient on MHD flow of a tri-hybrid Newtonian nanofluid in a circular channel. *J. Magn. Magn. Mater.* **2023**, *568*, 170320. [CrossRef]
12. Jin, K.; Qin, M.; Li, X.; Wang, R.; Zhao, Y.; Wang, H. Z-scheme Au@TiO_2/Bi_2WO_6 heterojunction as efficient visible-light photocatalyst for degradation of antibiotics. *J. Mol. Liq.* **2022**, *364*, 120017. [CrossRef]
13. Zhao, F.; Bai, Q.; Xia, C.; Hao, J.; Gayot, M.; Delville, J.-P.; Delville, M.-H. Core-shell nanoheterodimers: Laser-assisted deposition of single bimetallic Au@M (M = Au, Ag, Pd, Pt) nanodots on TiO_2 nanoparticles. *Mater. Adv.* **2022**, *4*, 694–708. [CrossRef]
14. Fontánez, K.; García, D.; Ortiz, D.; Sampayo, P.; Hernández, L.; Cotto, M.; Ducongé, J.; Díaz, F.; Morant, C.; Petrescu, F.; et al. Biomimetic Catalysts Based on Au@TiO_2-MoS_2-CeO_2 Composites for the Production of Hydrogen by Water Splitting. *Int. J. Mol. Sci.* **2022**, *24*, 363. [CrossRef]
15. Nazar, T.; Bhatti, M.M.; Michaelides, E.E. Michaelides, Hybrid (Au-TiO_2) nanofluid flow over a thin needle with magnetic field and thermal radiation: Dual solutions and stability analysis. *Microfluid. Nanofluidics* **2021**, *26*, 2. [CrossRef]
16. El Kot, M.A.; Elmaboud, Y.A. Elmaboud, Hybrid nanofluid flows through a vertical diseased coronary artery with heat transfer. *J. Mech. Med. Biol.* **2021**, *21*, 2150012. [CrossRef]
17. Zain, N.M.; Ismail, Z. Numerical solution of magnetohydrodynamics effects on a generalised power law fluid model of blood flow through a bifurcated artery with an overlapping shaped stenosis. *PLoS ONE* **2023**, *18*, e0276576. [CrossRef]
18. Mishra, N.K.; Sharma, M.; Sharma, B.K.; Khanduri, U. Soret and Dufour effects on MHD nanofluid flow of blood through a stenosed artery with variable viscosity. *Int. J. Mod. Phys. B* **2023**. [CrossRef]
19. Ashraf, M.U.; Qasim, M.; Shafie, S. Magnetohydrodynamic (MHD) Peristaltic flow of blood containing cylindrical shaped gold nanoparticles in a non-uniform tube in the presence of Joule dissipation. *J. Magn. Magn. Mater.* **2023**, *578*, 170708. [CrossRef]
20. Dharmaiah, G.; Prasad, J.R.; Balamurugan, K.; Nurhidayat, I.; Fernandez-Gamiz, U.; Noeiaghdam, S. Performance of magnetic dipole contribution on ferromagnetic non-Newtonian radiative MHD blood flow: An application of biotechnology and medical sciences. *Heliyon* **2023**, *9*, e13369. [CrossRef] [PubMed]
21. Cherkaoui, I.; Bettaibi, S.; Barkaoui, A.; Kuznik, F. Numerical study of pulsatile thermal magnetohydrodynamic blood flow in an artery with aneurysm using lattice Boltzmann method (LBM). *Commun. Nonlinear Sci. Numer. Simul.* **2023**, *123*, 107281. [CrossRef]
22. Kumar, P.G.; Prabakaran, R.; Sakthivadivel, D.; Thangapandian, N.; Velraj, R.; Kim, S.C. Effect of shot blasting on droplet contact angle of carbon aided phase change nanocomposites. *Surf. Eng.* **2021**, *37*, 1002–1011. [CrossRef]
23. Ramanuja, M.; Kavitha, J.; Sudhakar, A.; Radhika, N. Study of MHD SWCNT-Blood Nanofluid Flow in Presence of Viscous Dissipation and Radiation Effects through Porous Medium. *J. Niger. Soc. Phys. Sci.* **2023**, *14*, 1054. [CrossRef]
24. Yasin, M.; Hina, S.; Naz, R.; Hina, S. Influence of Hall and Slip on MHD Reiner-Rivlin blood flow through a porous medium in a cylindrical tube. *Res. Sq.* **2023**. [CrossRef]
25. Zahor, F.A.; Jain, R.; Ali, A.O.; Masanja, V.G. Modeling entropy generation of magnetohydrodynamics flow of nanofluid in a porous medium: A review. *Int. J. Numer. Methods Heat Fluid Flow* **2023**, *33*, 751–771. [CrossRef]
26. Jiang, X.; Hatami, M.; Abderrahmane, A.; Younis, O.; Makhdoum, B.M.; Guedri, K. Mixed convection heat transfer and entropy generation of MHD hybrid nanofluid in a cubic porous cavity with wavy wall and rotating cylinders. *Appl. Therm. Eng.* **2023**, *226*, 120302. [CrossRef]
27. Rajkumar, D.; Reddy, A.S.; Narayana, P.S.; Jagadeshkumar, K.; Chamkha, A.J. Pulsating magnetohydrodynamic flow of Fe_3O_4-blood based micropolar nanofluid between two vertical porous walls with Cattaneo–Christov heat flux and entropy generation. *J. Magn. Magn. Mater.* **2023**, *571*, 170564. [CrossRef]
28. Rehman, N.; Mahmood, R.; Majeed, A.H.; Rehman, K.U.; Shatanawi, W. Finite element analysis on entropy generation in MHD Iron(III) Oxide-Water NanoFluid equipped in partially heated fillet cavity. *J. Magn. Magn. Mater.* **2023**, *565*, 170269. [CrossRef]
29. Sahoo, A.; Nandkeolyar, R. Entropy generation in magnetohydrodynamic radiative non-Darcy slip flow of a Casson nanofluid with Hall effects and activation energy. *J. Magn. Magn. Mater.* **2023**, *575*, 170712. [CrossRef]

30. Tasnim, S.; Mitra, A.; Saha, H.; Islam, Q.; Saha, S. MHD conjugate natural convection and entropy generation of a nanofluid filled square enclosure with multiple heat-generating elements in the presence of Joule heating. *Results Eng.* **2023**, *17*, 100993. [CrossRef]
31. Khan, M.R.; Puneeth, V.; Alqahtani, A.M.; Alhazmi, S.E.; Beinane, S.A.O.; Shutaywi, M.; Eldin, S.M.; Alsenani, T.R. Numerical simulation and mathematical modeling for heat and mass transfer in MHD stagnation point flow of nanofluid consisting of entropy generation. *Sci. Rep.* **2023**, *13*, 1–21. [CrossRef]
32. Abuasbeh, K.; Ahmed, B.; Niazi, A.U.K.; Awadalla, M. Entropy Generation for MHD Peristaltic Transport of Non-Newtonian Fluid in a Horizontal Symmetric Divergent Channel. *Symmetry* **2023**, *15*, 359. [CrossRef]
33. Gandhi, R.; Sharma, B.K.; Makinde, O.D. Entropy analysis for MHD blood flow of hybrid nanoparticles (Au–Al_2O_3/blood) of different shapes through an irregular stenosed permeable walled artery under periodic body acceleration: Hemodynamical applications. *ZAMM Z. Fur Angew. Math. Und Mech.* **2022**, 1–29. [CrossRef]
34. Sharma, B.; Gandhi, R.; Bhatti, M. Entropy analysis of thermally radiating MHD slip flow of hybrid nanoparticles (Au-Al_2O_3/Blood) through a tapered multi-stenosed artery. *Chem. Phys. Lett.* **2022**, *790*, 139348. [CrossRef]
35. Gandhi, R.; Sharma, B.K.; Mishra, N.K.; Al-Mdallal, Q.M. Computer Simulations of EMHD Casson Nanofluid Flow of Blood through an Irregular Stenotic Permeable Artery: Application of Koo-Kleinstreuer-Li Correlations. *Nanomaterials* **2023**, *13*, 652. [CrossRef]
36. Tripathi, J.; Vasu, B.; Bég, O.A.; Gorla, R.S.R. Unsteady hybrid nanoparticle-mediated magneto-hemodynamics and heat transfer through an overlapped stenotic artery: Biomedical drug delivery simulation. *Proc. Inst. Mech. Eng. Part H J. Eng. Med.* **2021**, *235*, 1175–1196. [CrossRef]
37. Basha, H.T.; Rajagopal, K.; Ahammad, N.A.; Sathish, S.; Gunakala, S.R. Finite Difference Computation of Au-Cu/Magneto-Bio-Hybrid Nanofluid Flow in an Inclined Uneven Stenosis Artery. *Complexity* **2022**, *2022*, 2078372. [CrossRef]
38. Burton, A.C. *Physiology and Biophysics of the Circulation Introductory Text*; Year Book Medical Publisher: Chicago, IL, USA, 1966.
39. Zaman, A.; Ali, N.; Bég, O.A. Numerical study of unsteady blood flow through a vessel using Sisko model. *Eng. Sci. Technol. Int. J.* **2016**, *19*, 538–547. [CrossRef]
40. Ijaz, S.; Nadeem, S. Examination of nanoparticles as a drug carrier on blood flow through catheterized composite stenosed artery with permeable walls. *Comput. Methods Programs Biomed.* **2016**, *133*, 83–94. [CrossRef]
41. Box, G.E.P.; Wilson, K.B. On the Experimental Attainment of Optimum Conditions. *J. R. Stat. Soc. Ser. B (Methodol.)* **1951**, *13*, 1–38. [CrossRef]
42. Baskurt, O.K.; Hardeman, M.R.; Rampling, M.W.; Meiselman, H.J. *Handbook of Hemorheology and Hemodynamics, Biomedical and Health Research*; IOS Press: Washington, DC, USA, 2007; Volume 69, p. 468.